

AFRL-PR-WP-TR-1998-2111

**FUNDAMENTAL INVESTIGATIONS
OF AN INTEGRATED FUEL
INJECTOR/FLAMEHOLDER
CONCEPT FOR SUPERSONIC
COMBUSTION**



**MARK R. GRUBER
High Speed Systems Development Branch
Propulsion Sciences and Advanced Concepts Division
Air Force Research Laboratory
1950 Fifth Street
Wright-Patterson AFB OH 45433-7251**

19981120 182

SEPTEMBER 1998

FINAL REPORT FOR PERIOD JANUARY 1994 – JUNE 1997

APPROVED FOR PUBLIC RELEASE; DISTRIBUTION UNLIMITED

**PROPULSION DIRECTORATE
AIR FORCE RESEARCH LABORATORY
AIR FORCE MATERIEL COMMAND
WRIGHT-PATTERSON AIR FORCE BASE, OH 45433-7251**

NOTICE

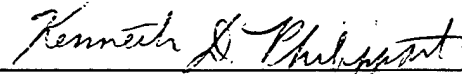
USING GOVERNMENT DRAWINGS, SPECIFICATIONS, OR OTHER DATA INCLUDED IN THIS DOCUMENT FOR ANY PURPOSE OTHER THAN GOVERNMENT PROCUREMENT DOES NOT IN ANY WAY OBLIGATE THE US GOVERNMENT. THE FACT THAT THE GOVERNMENT FORMULATED OR SUPPLIED THE DRAWINGS, SPECIFICATIONS, OR OTHER DATA DOES NOT LICENSE THE HOLDER OR ANY OTHER PERSON OR CORPORATION; OR CONVEY ANY RIGHTS OR PERMISSION TO MANUFACTURE, USE, OR SELL ANY PATENTED INVENTION THAT MAY RELATE TO THEM.

This technical report has been reviewed and is accepted under the provisions of the Small Business Innovative Research Program.

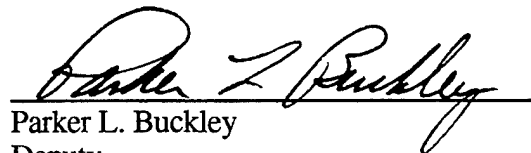
THIS REPORT IS RELEASABLE TO THE NATIONAL TECHNICAL INFORMATION SERVICE (NTIS). AT NTIS, IT WILL BE AVAILABLE TO THE GENERAL PUBLIC, INCLUDING FOREIGN NATIONS.



Mark R. Gruber, Ph.D.
Aerospace Engineer
High Speed Systems Development Branch



Kenneth D. Philippart, Maj. USAF
Chief
High Speed Systems Development Branch



Parker L. Buckley
Deputy
Propulsion Sciences and Advanced Concepts Division

If your mailing address has changed, if you wish to be removed from our mailing list, or if the addressee is no longer employed by your organization, please notify AFRL/PRSS Wright-Patterson OH 45433-7251 to help maintain a current mailing list.

Do not return copies of this report unless contractual obligations or notice on a specific document requires its return.

REPORT DOCUMENTATION PAGE			Form Approved OMB No. 0704-0188	
Public reporting burden for this collection of information is estimated to average 1 hour per response, including the time for reviewing instructions, searching existing data sources, gathering and maintaining the data needed, and completing and reviewing the collection of information. Send comments regarding this burden estimate or any other aspect of this collection of information, including suggestions for reducing this burden, to Washington Headquarters Services, Directorate for Information Operations and Reports, 1215 Jefferson Davis Highway, Suite 1204, Arlington, VA 22202-4302, and to the Office of Management and Budget, Paperwork Reduction Project (0704-0188), Washington, DC 20503.				
1. AGENCY USE ONLY (Leave blank)	2. REPORT DATE SEP 98	3. REPORT TYPE AND DATES COVERED FINAL MAY 96 - SEP 98		
4. TITLE AND SUBTITLE FUNDAMENTAL INVESTIGATIONS OF AN INTEGRATED FUEL INJECTOR/FLAMEHOLDER CONCEPT FOR SUPERSONIC COMBUSTION		5. FUNDING NUMBERS PE 61102F PR 2300 TA PO WU 04		
6. AUTHOR(S) MARK R. GRUBER				
7. PERFORMING ORGANIZATION NAME(S) AND ADDRESS(ES) High Speed Systems Development Branch Propulsion Sciences and Advanced Concepts Division Air Force Research Laboratory 1950 Fifth Street Wright-Patterson AFB OH 45433-7251		8. PERFORMING ORGANIZATION REPORT NUMBER		
9. SPONSORING/MONITORING AGENCY NAME(S) AND ADDRESS(ES) Propulsion Directorate Air Force Research Laboratory Air Force Materiel Command Wright-Patterson Air Force Base, OH 45433-7251 POC: Mark Gruber, AFRL/PRSS, 937-255-2175		10. SPONSORING/MONITORING AGENCY REPORT NUMBER AFRL-PR-WP-TR-1998-2111		
11. SUPPLEMENTARY NOTES				
12a. DISTRIBUTION AVAILABILITY STATEMENT Approved for public release; distribution is unlimited.			12b. DISTRIBUTION CODE	
13. ABSTRACT (Maximum 200 words) This report describes the results of a recent series of experiments designed to examine the fundamental behavior of several cavity-based flameholder candidates in a non-reacting supersonic flow. Seven geometries were tested in conjunction with a new facility nozzle. Results indicate that the cavity aft ramp plays a strong role in determining the character of the shear layer which spans the length of the cavity. For rectangular cavities, a compression wave forms as the flow separates from the upstream corner of the cavity. Thus, the pressure on the upstream face increases above the freestream value. In these cases, the recompression which occurs at the aft wall is very sharp with strong pressure gradients at the axial location corresponding to the aft wall. These cases are also visibly unsteady. Reductions in the ramp angle yield more stable, two-dimensional flowfields. However, the character of the separation wave changes gradually from compressive to expansive as the ramp angle is reduced. As such, the shear layer tends to dip into the cavity and the recompression occurs more gradually as the shear layer reattaches to the aft wall. Changes in cavity offset ratio result in more dramatic changes in the cavity flowfield. The separation wave becomes strongly expansive leading to severe shear layer intrusion into the cavity. Aft wall changes do not strongly impact the character of the shear layer, although stability is enhanced and recompression is more gradual for shallower ramp angles.				
14. SUBJECT TERMS SCRAMJET, FUEL INJECTION, FLAMEHOLDER, SUPERSONIC COMBUSTION			15. NUMBER OF PAGES 54	
			16. PRICE CODE	
17. SECURITY CLASSIFICATION OF REPORT UNCLASSIFIED	18. SECURITY CLASSIFICATION OF THIS PAGE UNCLASSIFIED	19. SECURITY CLASSIFICATION OF ABSTRACT UNCLASSIFIED	20. LIMITATION OF ABSTRACT SAR	

Table of Contents

List of Tables	iv
List of Figures	v
Abstract	vii
1. Introduction	1
2. Literature Review.....	3
3. Experimental Facility.....	6
4. Mach 3 Nozzle Design and Calibration	8
4.1 Design	8
4.2 Calibration	8
5. Cavity-Based Flameholder Model Designs.....	11
6. Experimental Results.....	14
6.1 Visualization Results	14
6.2 Wall Pressure Data.....	16
7. Conclusions.....	20
Tables	22
Figures.....	28
References	46

List of Tables

Table 4.1 Mach 3 Nozzle Contour Coordinates	22
Table 5.1 Cavity Geometry Specifications.....	24
Table 5.2 Cavity Instrumentation Locations	24

List of Figures

Figure 2.1 Character of Cavity Flows (a) Open Cavity Flow, (b) Closed Cavity Flow.....	28
Figure 3.1 Room 19 Facility Schematic	28
Figure 4.1 Mach 3 Nozzle Contour	29
Figure 4.2 Mach 3 Nozzle Installed in Room 19	29
Figure 4.3 Mach 3 Nozzle Normalized Sidewall Pressure Distributions (a) Stagnation Pressure = 20 psia, (b) Stagnation Pressure = 100 psia, (c) Stagnation Pressure = 125 psia.....	30
Figure 4.4 Pitot Pressure Distributions at $x = 13.5''$ Downstream of Nozzle Exit (Stagnation Pressure = 100 psia) (a) Core Region, (b) Near-Wall Region	31
Figure 4.5 Shadowgraph Photo from Clean Test Section (Flow is Left to Right).....	32
Figure 4.6 Shadowgraph Photo of Circular Jet in Crossflow	32
Figure 5.1 Cavity Geometry Schematic.....	33
Figure 5.2 Photographs of Cavity Models (a) LD3-O1, (b) LD3-O1-16, (c) LD3-O1-30, (d) LD3-O2, (e) LD3-O2-16, (f) LD5-O1, (g) LD5-O1-16.....	33
Figure 5.3 Representative Cavity Assembly Drawing (LD3-O1)	34
Figure 6.1 Visualizations of LD3-O1 (a) Shadowgraph Photo, (b) Schlieren Photo.....	35
Figure 6.2 Visualizations of LD3-O1-16 (a) Shadowgraph Photo, (b) Schlieren Photo	36
Figure 6.3 Visualizations of LD3-O1-30 (a) Shadowgraph Photo, (b) Schlieren Photo	37
Figure 6.4 Visualizations of LD3-O2 (a) Shadowgraph Photo, (b) Schlieren Photo.....	38
Figure 6.5 Visualizations of LD3-O2-16 (a) Shadowgraph Photo, (b) Schlieren Photo	39
Figure 6.6 Visualizations of LD5-O1 (a) Shadowgraph Photo, (b) Schlieren Photo.....	40
Figure 6.7 Visualizations of LD5-O1-16 (a) Shadowgraph Photo, (b) Schlieren Photo	41
Figure 6.8 Wall Static Pressure Distribution for LD3-O1	42
Figure 6.9 Wall Static Pressure Distribution for LD3-O1-16.....	42
Figure 6.10 Wall Static Pressure Distribution for LD3-O1-30.....	43
Figure 6.11 Wall Static Pressure Distribution for LD3-O2.....	43
Figure 6.12 Wall Static Pressure Distribution for LD3-O2-16.....	44

Figure 6.13 Wall Static Pressure Distribution for LD5-O1	44
Figure 6.14 Wall Static Pressure Distribution for LD5-O1-16.....	45

Abstract

This report describes the results of a recent series of experiments designed to examine the fundamental behavior of several cavity-based flameholder candidates in a non-reacting supersonic flow. The cavity geometries considered were all of the open type. Two length-to-depth ratios were studied while offset ratio and aft ramp angle were systematically varied. Measurements included conventional visualizations and wall static pressures from upstream of and within the cavity. Also included herein is a calibration of a new facility nozzle for AFRL/PRSS Test Cell 19.

The new facility nozzle was found to operate cleanly with relatively small disturbances to the freestream flow. The nozzle behavior was independent of operating conditions and pitot probe results showed a spatially uniform core flow with a well-behaved boundary layer on the test section lower wall. Nozzle pressure data were spanwise symmetric and collapsed for a wide range of stagnation pressures.

Seven cavity geometries were tested in conjunction with the new facility nozzle. Results indicate that the aft ramp angle plays a strong role in determining the character of the shear layer which spans the length of the cavity. For rectangular cavities (i.e., aft ramp angle = 90°), a compression wave forms as the flow separates from the upstream corner of the cavity. Thus, the pressure on the upstream face increases above the freestream value. In these cases, the recompression which occurs at the aft wall is very sharp with strong pressure gradients at the axial location corresponding to the aft wall. These cases are also visibly unsteady as evidenced in the flow visualizations by the periodic waves which interact with the main separation and recompression shocks. Reductions in the aft ramp angle below 90° yield more stable, two-dimensional flowfields. However, the character of the separation wave changes from compressive (in the $\theta = 90^\circ$ and 30° cases) to expansive (in the $\theta = 16^\circ$ case). As such, the pressure on the upstream face of the cavity steadily decreases as the ramp angle decreases. The shear layer tends to dip into the cavity for these cases and the recompression occurs more gradually as the shear layer reattaches to the cavity aft wall.

Changes in the offset ratio cause more drastic changes to the cavity flowfield. First, the separation wave is observed to be relatively strong and expansive in nature. The upstream face of the cavity experiences a much lower pressure in these cases than in any of the configuration where offset ratio is unity. The shear layer dips much further into the cavity. The aft ramp angle has less influence on the overall cavity performance in these cases: no appreciable change in the pressure at the upstream face occurred as the ramp angle was decreased from 90° to 16° . Of course, the recompression wave structure changed slightly in response to the angle aft ramp.

1. Introduction

Fuel injection and flameholding present fundamental challenges to the design and implementation of a supersonic combustion ramjet (scramjet) engine. A successful fuel injection scheme must provide rapid mixing between the fuel and air streams. However, the introduction of fuel into the oxidizing stream must be carried out in such a way that the oxidizing stream suffers acceptable total pressure losses. Another technical challenge associated with combustion in supersonic environments is to provide a stable flameholding system. Finally, due to the harsh thermal loading inherent in a scramjet combustor, an active cooling system may be required for maintaining the life of the fuel injection/flameholding scheme.

Although scramjet research began in the early sixties, to date, these problems have not been adequately resolved. Several flush wall injection concepts have been investigated that provide relatively fast mixing between the fuel and air streams. However, these techniques can introduce large penalties due to potentially high total pressure losses (caused by strong shocks) and severe wall cooling requirements. Strut injection concepts have also been studied. These geometries produce a wake region that inherently promotes flameholding. Total pressure losses are relatively small, and, if the fuel stream is aligned with the combustor axis, a significant portion of the engine thrust is obtained from the momentum of the injected fuel. However, the mixing between the fuel and air is relatively slow and fuel dispersal into the oxidizing stream is limited to the wake region created by the strut. A clear need exists for the development of a system that effectively integrates fuel injection and flameholding for supersonic combustion. Such a device would contribute significantly to the present research and industrial technology base.

The investigation documented herein is the first of a multiple step approach aimed at improving the fundamental understanding associated with effective flameholding in supersonic flows. The baseline concept uses a wall cavity to provide the stabilization zone for the reactions. This cavity is characterized by several geometric parameters including its length-to-depth ratio (L/D), its aft ramp angle (θ), and its offset ratio (OR). Absolute magnitudes of length and depth are also of interest. Fuel injection may be easily incorporated into this device in a variety of

locations from inside to upstream to downstream. The effectiveness of the device will most likely depend on its entrainment rate and its characteristic residence time.

Initially, simple models of the proposed system are experimentally studied at one freestream Mach number to identify the important issues in the design of such a device. Shadowgraph and schlieren photographs are used to investigate the qualitative features of the flowfield. Measurements of wall static pressures throughout the device are also be obtained. These data will be particularly useful in validating computer codes used to model such flowfields. Additional measurements will be made in the second phase of this project including residence time, entrainment rate, pressure fluctuations, and the velocity field surrounding the device. The third phase of the project involves the introduction of fuel and assessments of combustion stability, mixing effectiveness, pressure loss, and combustion efficiency.

2. Literature Review

Three recent publications have presented relatively comprehensive literature surveys on the subject of cavity flows and their relevance for flameholders in supersonic combustion engines.¹⁻³ Experimental and analytical research to date has predominantly been in the area concerning the role of cavities in external flows (i.e., as wheel wells or bomb bays on supersonic aircraft),⁴⁻²⁴ although there have been studies examining the flameholding characteristics in low speed²⁵⁻²⁸ and high speed flows.^{1-3,29,30} Several Russian researchers have also demonstrated the usefulness of cavities in high speed combustion applications.³¹⁻³⁵

In general, cavity flows fall into one of two categories: open or closed. These two flowfields are shown schematically in Fig. 2.1. In open cavity flows, the shear layer formed at the separation corner spans the entire cavity length and reattaches somewhere along the cavity back face. Closed cavity flows occur when the shear layer is unable to span the entire length of the cavity and reattaches on the cavity floor. Closed cavities are characterized by larger drag coefficients compared to open cavities; therefore, due to the high penalty of internal drag in a scramjet combustor, open cavities are more desirable. The length-to-depth ratio (L/D) that divides open from closed behavior is between 10 and 12.³⁶ In addition to this operational transition, another interesting feature of cavity flows involves the mode by which acoustic waves propagate inside the cavity. Zhang and Edwards²¹ have found that for very small values of L/D , a cavity immersed in a supersonic stream is dominated by the transverse mode where acoustic waves propagate perpendicularly with respect to the crossflow. As L/D increases, the oscillation mode changes to one where the waves travel along the length of the cavity (i.e., parallel to the crossflow). This mode is termed longitudinal. The transition between the transverse and longitudinal modes results in a sudden increase in the cavity form drag coefficient. After establishment of the longitudinal mode, the form drag coefficient decreases slightly with increasing L/D before increasing dramatically due to the effects of stronger shear layer recompression on the aft face.

In their low speed combustion work, Hsu et al.²⁶ directly injected fuel and air into an axisymmetric cavity to achieve flame stabilization. Their cavity was characterized by an offset

ratio of approximately 1.4 and a variable length-to-depth ratio. Stable flames were shown to result for cavity lengths between 0.45 and 0.65 aft wall diameters. Longer cavities produced vortex shedding that resulted in unstable flames, while shorter cavities did not provide enough air entrainment to hold the flame. One key conclusion from their work was that the principal driver for cavity size was minimum drag. The presence or absence of combustion did not influence the sizing. CFD calculations were performed on this cavity geometry and similar results suggesting a limited range of lengths for achievement of a stable flame zone.^{27,28}

Yu et al.³⁰ studied a variety of cavity configurations in an unheated (i.e., ambient temperature) high speed (Mach 2) flow. The effort was directed at investigating the influence of cavity geometry on the combustion of a fuel jet injected upstream of the cavity. Their results suggested that small aspect ratio cavities may provide more flameholding capability than longer cavities with inclined aft ramp angles. Similar work has been in progress at the Air Force Research Laboratory for some time, where room temperature ethylene is injected upstream of a relatively long cavity (with an angled aft ramp) being used to stabilize flames in a supersonic combustor at conditions simulating flight Mach numbers between 4 and 6 and flight dynamic pressures between 1000 and 2000 lb/ft².³⁷ Though unpublished at the present time, recent results indicate, contrary to the work the Yu et al.,³⁰ that very good flameholding is provided by the cavity and, moreover, flame spreading is quite significant.³⁸

Given the relatively small amount of information aimed at understanding the fundamental aspects of cavities as flameholders in supersonic flows, a research project was initiated to provide some insight into this problem. Based on the previous work discussed above, the drag associated with the cavity flameholder is a key consideration in its design as are the entrainment rate into the cavity and the residence time within the cavity. The current work focuses on fundamental characterizations of a variety of cavity geometries where influences of L/D, offset ratio, and aft wall ramp angle on the flowfield are investigated. Included in the initial work are measurements of the wall static pressure distribution upstream of and throughout the cavity model. These measurements may be used to estimate the drag produced by the cavity. These data may also be

used to compare directly with CFD results to validate the accuracy of the CFD model for this flowfield. Also, conventional visualizations are carried out to understand the features which govern the flowfield. This report compiles these results after brief descriptions of the test facility and the specific hardware (Mach 3 facility nozzle and the seven cavity geometries) which was designed and constructed for these experiments.

3. Experimental Facility

The experiments in this report were conducted in the continuous flow supersonic facility located at the Air Force Research Laboratory, Propulsion Directorate, Propulsion Sciences and Advanced Concepts Division, High Speed Systems Development Branch (AFRL/PRSS). This facility is designed to allow studies of the basic fluid dynamic mechanisms that govern fuel-air mixing in supersonic combustors using conventional and state-of-the-art non-intrusive diagnostic techniques. A schematic of the facility appears in Fig. 3.1. Hot and cold air lines supply compressed air at up to 1660°R and ambient temperature, respectively, for a total flow rate of about 30 lb_m/s at 750 psia. Elevated temperatures are provided by a gas fired heat exchanger. The two lines merge in an insulated expansion loop that carries the resulting warm air to the supersonic wind tunnel mounted inside a clean room with a controlled atmosphere.

After entering the clean room, the air travels to the settling chamber through a pair of manifolds, a shut-off valve, and an expansion section (see Fig. 3.1). A rearward-facing perforated cone spreads the flow during the sudden expansion to fill the 24 inch diameter settling chamber. This chamber conditions the air using an array of mesh screens and a section of honeycomb to break up large scale turbulence and straighten the flow before acceleration by the supersonic nozzle. Pressure and temperature sensors installed in the settling chamber record operating conditions and provide control system feedback.

Planar two-dimensional converging-diverging nozzles, designed using a method of characteristics code,³⁹ produce the desired expansion to a specified Mach number at the entrance to the test section. An empirical correction⁴⁰ applied to the contoured walls of the nozzle preserves the parallel nature of the side walls and makes the nozzle exit dimensions 5.16 inches high by 6.0 inches wide. The side walls of the nozzle section house pressure taps on the transverse center plane allowing documentation of the centerline wall pressure distribution from the nozzle entrance through the throat to the exit.

The constant area test section requires a large degree of optical access so that a wide variety of non-intrusive diagnostic techniques may be used to examine the flow. A pair of fused silica

windows mounted in the side walls and a single fused silica window mounted in the top wall provide the necessary access. A total viewing length of 31 inches results in the streamwise dimension of the test section. Additionally, the entire transverse dimension and half of the spanwise dimension are directly accessible through the side and top windows, respectively. Further details regarding the facility are available elsewhere.^{41,42}

Two principal diagnostic techniques were used in this investigation: line of sight visualization (i.e., shadowgraph and schlieren photography) and wall static pressure measurements. Shadowgraph and schlieren photography are conventional technique whereby in-stream density gradients are visualized. A Xenon nanolamp (pulse duration ~10 ns) effectively freezes the flowfield, and a PixelVision unintensified CCD camera records the spatially integrated visualizations. The camera is controlled using a Pentium-PC and the recorded images are stored for further analysis. This system reveals the dominant features of the flow surrounding the cavity-based flameholder as well as any undesirable wave phenomenon present within the test section. The schlieren configuration had the knife edge oriented horizontally so that changes in density in the transverse direction were observed. Pressure measurements are obtained from several locations throughout the test section including the wall opposing the cavity-based flameholder and inside the cavity model itself. These measurements are made using traditional pressure taps (~0.031 inches in diameter) to sense the mean wall static pressure distribution at the tap location. The taps are connected to a multi-channel Pressure Systems Incorporated (PSI) system and are recorded using a custom-built computer-controlled data acquisition system.

4. Mach 3 Nozzle Design and Calibration

As part of this research, the design, construction, and calibration of a new Mach 3 facility nozzle for Test Cell 19 was required. The sections that follow describe the design procedure and the results of calibration experiments.

4.1 Design

The design methodology for this nozzle consisted of three parts. First, a computer code was used to calculate the inviscid nozzle contour based on the method of characteristics.³⁹ This code has been used to design nozzles for this facility in the past with very good success. The second step involves the application of an appropriate correction to the inviscid contour which accounts for viscous effects. This is accomplished using Burke's equation,⁴⁰ which relates the local turbulent boundary layer displacement thickness to the local Mach and Reynolds numbers as follows:

$$\frac{\delta_x^*}{x} = 0.0463 \frac{M_x^{1.311}}{\text{Re}_x^{0.276}}$$

Finally, the converging portion of the contour is determined. Two curves were used to produce a gentle transition from the nozzle inlet to the throat. A circular arc was prescribed to be tangent to the nozzle throat while a parabolic arc was fitted to the inlet. These two curves met at a point upstream of the throat where their slopes were equal such that a smooth contour was produced. The resulting nozzle contour is shown in Fig. 4.1 with coordinates given in Table 4.1. A photograph of the nozzle blocks installed in the test facility appears in Fig. 4.2. Flow in this photo would be from left to right.

4.2 Calibration

Once installed into the facility, the nozzle performance must be calibrated to ensure proper operation. Several techniques may be used for this calibration including wall static pressure

measurements, in-stream probe measurements, and flow visualization. Each of these techniques was applied to verify the performance of the Mach 3 nozzle prior to its use in the cavity-based flameholder experiments.

Wall static pressure data were collected from the two nozzle sidewalls for three facility inlet conditions. These data appear in Fig. 4.3 for $p_o = 20, 100, \text{ and } 125 \text{ psia}$; excellent spanwise symmetry is observed. The isentropic relation shown below may be used to compute the nozzle exit Mach number for each stagnation pressure condition.

$$\frac{p_o}{p} = \left(1 + \frac{\gamma - 1}{2} M^2 \right)^{\gamma/(\gamma - 1)}$$

This calculation produces $M = 2.94, 2.92, \text{ and } 2.92$ for $p_o = 20, 100, \text{ and } 125 \text{ psia}$, respectively.

A pitot probe was used to probe the flow at a streamwise location of 13.5 inches downstream of the nozzle exit. For these measurements, the stagnation pressure was approximately 100 psia. The main goal of the in-stream measurements was to examine flow uniformity inside the test section. Figure 4.4 presents the results of these probe measurements. Pitot pressure is plotted on a two-dimensional grid as if the flow were exiting out of the page. Figure 4.4a shows the entire cross-sectional area of the test section. Wall effects are clearly visible at $z = \pm 3.0$ inches, but aside from these regions, the core flow appears quite uniform. The boundary layer on the lower wall is shown in Fig. 4.4b. Here again, spanwise symmetry (i.e., about the z direction) is clearly evident. From these examinations of wall static pressure and pitot pressure, it is concluded that the new facility nozzle is producing a uniform stream at approximately $M = 2.93$.

In addition to the pressure measurements, several spark shadowgraph photos were collected from the test section with various fuel injector models installed. First, the clean test section was examined. A shadowgraph from the stations nearest the nozzle exit is shown in Fig. 4.5. In this figure, flow is from left to right and the bottom wall boundary layer is clearly observed. Several weak waves emanating from various interfaces in the test section are present,

but none of these waves appears very strong. In fact, the flowfield produced by sonic injection of air through a single normal circular fuel injector appears undisturbed by the waves present in the test section (see Fig. 4.6). Other fuel injectors were also examined (e.g., a swept ramp fuel and a nine-hole fuel injector array). These also appeared uninfluenced by the waves in the test section. The shadowgraph photos shown provide good indications that the facility nozzle is performing satisfactorily.

5. Cavity-Based Flameholder Model Designs

As presented in the literature review contained in §2, a variety of cavity geometries have been investigated both experimentally and computationally. Many of these studies were focused largely on issues surrounding external flows (e.g., bomb bay doors on aircraft) while some recent attention has been paid to the cavity as a flameholder inside aircraft engines. As a result of these studies, several geometric parameters have surfaced as being important. Namely, since the shear layer formed across the cavity opening plays a dominant role in the performance of the device, the length-to-depth ratio (L/D) is of importance. Studies have shown that large L/D yields a “closed” cavity with relatively high drag compared to lower L/D due to shear layer impingement on the cavity bottom wall. Minimization of internal drag is very important in scramjet combustors; thus, large L/D cavities should probably be avoided. Cavity length, however, contributes to the entrainment of fluid into the cavity via diffusion across the shear layer. Therefore, a significant trade-off appears. That is, if the cavity is to sustain a flame, it requires fuel and air to be present in the correct proportions for combustion. Longer cavities lead to higher levels of entrainment, but also drag. Additional parameters of interest include the aft ramp angle (θ) and the ratio of upstream step height to aft step height (i.e., offset ratio (OR)). The ramp angle has been shown to influence the acoustic stability of the cavity by providing the shear layer a more stable location on which to reattach. A non-unity offset ratio has also been shown to be effective in low speed combustors for flameholding²⁶⁻²⁸ and in missile afterbodies for drag reduction.⁴³

Due to the severe drag penalties that appear to accompany cavities with $L/D \geq 10$, the present investigation focused on “open” cavities while allowing a wide variation of θ and OR. The matrix shown in Table 5.1 highlights the main features of the models which were designed and constructed for these experiments. Two length-to-depth ratios were selected ($L/D = 3$ and 5). Five models were built with $L/D = 3$: two rectangular cavities (one with $OR = 1$ and one with $OR = 2$), two non-rectangular cavities with unity offset ratio ($\theta = 16^\circ$ and 30°), and one non-rectangular cavity with non-unity offset ratio ($\theta = 16^\circ$ and $OR = 2$). Two $L/D = 5$ models were

built: one rectangular and one non-rectangular ($\theta = 16^\circ$) each with $OR = 1$. All models have the same depth ($D_u = 0.35$ inches) and the length is defined as shown in Fig. 5.1.

The seven models are shown pictorially in Fig. 5.2. Each name specifies the geometry of the model (i.e., LD3-O2-16 corresponds to $L/D = 3$, $OR = 2$, $\theta = 16^\circ$). The flow direction in these pictures is from left to right. Each test article is comprised of six pieces (five of which are shown in the pictures). All cavities span the entire test section. To obtain good optical access into the cavities, they must be elevated into the field of view of the window. This task is accomplished using the forward ramp, which turns the flow 10° toward centerline and then back parallel to the main flow direction. The ramp mounts directly onto one of the replaceable blocks in the test section bottom wall. Just downstream of this ramp is a small piece that forms the upstream face of the cavity. This piece is common to all cavity geometries and was made separate from the ramp to allow instrumentation and fuel injectors to be placed in the backstep. The next piece aft defines the cavity geometry. All geometric variations are accomplished using this piece (i.e., seven aft pieces exist to yield the seven specific geometries of interest). An array of instrumentation and fuel injection ports are available in these pieces. These two pieces are mounted together onto another of the replaceable test section blocks. Finally, a flat plate is attached just downstream of the cavity model to isolate it from any downstream disturbance. This plate is absent from Fig. 5.2.

A schematic of the cavity assembly appears in Fig. 5.3. This sketch details the location of the hardware inside the test section with respect to the facility nozzle exit. It also shows the individual pieces which comprise the assembled cavity (i.e., the forward ramp, the upstream cavity face plate, and the aft cavity). As in the photos presented above, the aft flat plate is not shown in this schematic.

The cavity models are instrumented with several wall static pressure taps; the locations of these taps are shown in Table 5.2. In this table, the x-y-z coordinate origin corresponds to the upstream separation corner of the cavity on the cavity spanwise centerline. By placing several taps across the span of the cavity at many axial locations, the two-dimensionality of the pressure field may be assessed. Additionally, pressure taps are concentrated on the spanwise centerline of the

cavity geometries to capture as many features of the pressure distribution as possible for use with CFD code validation.

6. Experimental Results

The Mach 3 facility nozzle was operated at a stagnation pressure of 100 psia and a stagnation temperature of 540°R for all of the cavity model experiments discussed below. Instantaneous shadowgraph and schlieren photographs of the flowfield about each cavity model are shown. Following these results, the wall static pressure data are presented and discussed.

6.1 Visualization Results

Figures 6.1-6.7 show shadowgraph and schlieren photos of the flowfield about each of the seven cavity geometries studied in this investigation. The flow direction in all the photos is from left to right. The scale of the photos is approximately 75% of full scale. Several features are common to all the photos including the shock generated by the forward ramp that interacts with the boundary layer on the upper wall (top of photographs). This interaction is clearly visible and the wave generated as a result of the interaction can also be clearly observed. The region above the cavity models is essentially free from other disturbances that would produce confounding effects on the cavity itself. Each photo also shows a relatively weak wave generated at the interface between the forward ramp and the cavity upstream face plate. This wave does not appear to impact the dynamics of the cavity flow.

The visualizations obtained from model LD3-O1 are presented in Fig. 6.1. In these photos, it appears that the approaching boundary layer thickness is roughly on the order of the cavity depth. Several interesting features are present in these two photos. First, the wave formed at the separation point on the cavity upstream face appears compressive in nature. An expansion wave would appear lighter than the main flow in a schlieren photograph due to the acceleration of the flow and concomitant decrease in density. However, in Fig. 6.1b, this wave appears dark indicative of a compression wave. Close examination of the two photos does suggest that the shear layer formed atop the cavity actually lifts above the floor confirming that the flow is compressed slightly as it separates from the corner of the upstream face plate. Another interesting feature in these photos is the curved nature of the waves generated by the cavity. This suggests an

oscillatory behavior. Patterns of this type have been recently observed in computations by Zhang,²⁴ where a cavity with $L/D = 3$ was studied in a Mach 2.5 stream. The oscillations were determined to be related to the oscillatory vortex structure within the cavity. The recompression wave at the aft corner of the cavity is also clear. This feature appears to interact with other oscillatory disturbances generated as a result of the cyclic cavity vortex structure.

Results from model LD3-O1-16 appear in Fig. 6.2. Here, in contrast with the photos shown in Fig. 6.1, the oscillatory nature of the waves generated by the cavity is not present. This indicates the relative steadiness of the flowfield about this cavity. Also of note is the character of the wave at the separation corner. For this geometry, this is an expansion wave (as indicated in the schlieren photo by its light color). The shear layer that spans the cavity has a slight declination downward and the recompression point is below the level of the floor. The recompression wave appears stronger in this case compared to LD3-O1 and the flowfield generally appears more stable and two-dimensional.

The effects of increasing the aft ramp angle to 30° for a fixed length-to-depth ratio can be seen in Fig. 6.3. The wave emanating from the separation corner now appears to be compressive in nature and the shear layer is not as inclined to the main flow direction as in Fig. 6.2. The recompression point appears to have moved upward along the aft ramp and the recompression wave strength is similar to that in Fig. 6.2. Similar stability and two-dimensionality are observed with this model as with LD3-O1-16.

By changing the offset ratio of the cavity, some very interesting features develop in the flowfield. Figure 6.4 shows the shadowgraph and schlieren photos from the LD3-O2 geometry. The most obvious observation in these photos is the very strong expansion fan generated at the separation corner. This is expected because of the displacement of the aft wall beneath the forward wall. The shear layer immediately becomes angled with respect to the main flow direction and appears to experience recompression very near the aft corner of the cavity. The flow over this cavity appears very steady in comparison with LD3-O1 suggesting that increasing the offset ratio

influences the behavior of the vortex structure within the cavity that leads to the oscillatory behavior in rectangular cavities with unity offset ratio.

When the aft ramp is inclined at 16° , the flowfield associated with the $OR = 2$ cavity becomes much like that of LD3-O1-16 with the exception of a much stronger expansion fan at the separation corner. Figure 6.5 shows the representative shadowgraph and schlieren photos from this geometry. The recompression wave again appears stronger in the case with the 16° aft ramp compared to the 90° aft ramp (compare Figs. 6.4 and 6.5). Also, the flow again appears quite steady in that no discernible curvature of the shock waves is present (recall Fig. 6.1 for the LD3-O1 case).

All of the visualizations presented thus far were obtained with the $L/D = 3$ geometries. When the L/D is increased to 5 in a rectangular cavity, the photos presented in Fig. 6.6 result. Here, the shear layer that spans the cavity is slightly inclined with respect to the flow direction and the compression wave at the separation corner returns. Some cavity oscillations are present as evidenced by the curved waves formed between the separation and recompression waves.

Results from model LD5-O1-16 appear in Fig. 6.7. Here, oscillatory waves are again absent indicating a relatively steady flowfield about the cavity. The wave at the separation corner is an expansion wave (as indicated in the schlieren photo by its light color) of similarly strength to the one formed in LD3-O1-16. The shear layer that spans the cavity has a slight declination and the recompression point is again below the level of the floor. The recompression wave appears stronger in this case compared to LD5-O1.

6.2 Wall Pressure Data

Figures 6.8-6.14 present the mean wall static pressure distributions measured for each cavity geometry. In each figure, the static pressure is plotted as a function of the axial distance. This distance is measured from the cavity upstream face. The three measurement locations upstream of the face correspond to the three taps installed in the forward ramp. Multiple

measurements are presented at several locations where taps were installed off the spanwise centerline to assess the two-dimensionality of the cavity flowfield.

The results from LD3-O1 appear in Fig. 6.8. As noted in the discussion of the visualizations from this geometry, a compression wave is situated at the separation corner ($x = 0$) thereby resulting an increase in pressure into the cavity. A gradual decrease in pressure is noticed along the cavity bottom wall until the aft face is approached. At this location, the shear layer which spans the cavity experiences recompression leading to the higher pressure level on the aft face of the cavity (at $x = 1.05''$). It is anticipated that the resolution of the pressure taps is insufficient to capture all the activity from inside the cavity. For example, the region near the aft face of the cavity is expected to be characterized by strong gradients due to the standing vortex which forms close to the cavity bottom wall. The current measurements do not display any such gradients and they also only capture one measurement on the aft face. The recompression has been shown to via computer simulation to be rather strong. It is hoped that these experimental data will, however, validate the CFD predictions over a large portion of the cavity geometry. A final note regarding Fig. 6.8 is that the data from the aft ramp appear relatively two-dimensional about the span (i.e., the four measurements from $x = 1.05''$ fall nearly atop one another).

The data presented in Fig. 6.9 are from LD3-O1-16. In this geometry, the pressure on the upstream face of the cavity appears to be reduced compared to that shown in Fig. 6.8. This agrees with the interpretation from the visualizations presented above that showed an expansion wave forming at the separation corner. The pressure along the cavity floor is essentially constant at the same level as that of the upstream face. Recompression occurs on the 16° ramp leading to locally high pressure levels. Throughout this flowfield, the spanwise symmetry is consistent indicating a high degree of two-dimensionality.

As the aft angle is increased to 30° , several changes take place as shown in Fig. 6.10. First, the wave emanating from the separation corner causes the pressure on the upstream face to increase slightly above the level just upstream. Thus, as noted in the visualizations, this wave is compressive in nature as opposed to the expansion wave observed in LD3-O1-16 (Figs. 6.2 and

6.9). The behavior within the cavity appears similar to that shown in Fig. 6.9 although at a slightly elevated pressure. Finally, the recompression caused as the shear layer reattaches onto the ramp occurs more quickly (i.e., the gradient dp/dx is much steeper in LD3-O1-30 than in LD3-O1-16). It is thought that the steeper ramp angle results in a cavity that behaves more closely to the rectangular cavity (LD3-O1). Once again, the pressure data from the taps placed off the cavity centerline collapse well suggesting a high degree of two-dimensionality over this distance.

Figure 6.11 presents the pressure distribution measured from the rectangular $L/D = 3$ cavity with an $OR = 2$. In this case, the change to the downstream step height has significantly impacted the pressure distribution. The expansion wave emanating from the separation corner is much stronger than any experienced in the unity offset ratio geometries. In this case, the pressure on the upstream face of the cavity has fallen below 2 psia compared to around 3 psia for the previous cavities. The pressure on the lower wall of the cavity appears to drop slightly as the flow approaches the aft wall, where recompression again occurs. The collapse of the data from multiple spanwise stations appears excellent indicating that the flow is relatively two-dimensional over this distance (approximately $0.75''$ or just over two upstream step heights).

Figure 6.12 shows the effects of decreasing the ramp angle from 90° (i.e., rectangular) to 16° in the LD3-O2 geometry. It appears that the effects are largely confined to the recompression region on the aft wall. The expansion from the separation corner appears uninfluenced by the change made to the ramp angle as indicated by the pressure on the upstream face remaining unchanged from LD3-O2 to LD3-O2-16. Two-dimensionality is again apparent from the collapse of the data obtained from off the centerline. The very low pressure level on the upstream face suggests a relatively large form drag associated with the $OR = 2$ cavity geometries.

By increasing the cavity length while holding the depth constant, the L/D is increased. Figure 6.13 shows the results of increasing the L/D to 5 in a rectangular geometry with $OR = 1$. Several features are notable when comparing this pressure distribution to the one shown in Fig. 6.8 for the LD3-O1 cavity. First, the compression wave emanating from the separation corner is stronger in LD5-O1 as suggested by the higher pressure level on the upstream face of the cavity.

The lower cavity wall appears to be at roughly constant pressure until the aft wall where the vortex structure results in a pressure rise. Finally, recompression yields a higher pressure on the aft wall than in Fig. 6.8. At this location, the off-centerline pressures do not exhibit the same degree of collapse as in earlier geometries studied. This would indicate that the LD5-O1 cavity is not as two-dimensional as others, at least near the shear layer reattachment point.

Finally, the pressure distribution from LD5-O1-16 is presented in Fig. 6.14. In this case, the expansion wave present at the separation corner is of similar strength to the one generated by LD3-O1-16 as inferred from the pressure level on the upstream face of the cavity. The pressure distribution along the cavity bottom wall is relatively constant and recompression appears slightly stronger than in LD3-O1-16. Thus, for a fixed cavity depth, offset ratio, and aft wall ramp angle, the increased length appears to increase the pressure in the recompression region while no influence is observed on the upstream face of the cavity. Therefore, the form drag created by LD5-O1-16 is somewhat higher than that of LD3-O1-16. However, since the shear layer length has increased, it is expected that the entrainment of freestream fluid into the longer cavity should increase.

7. Conclusions

This report describes the results of a recent series of experiments designed to examine the fundamental behavior of several cavity-based flameholder candidates in a non-reacting supersonic flow. The cavity geometries considered were all of the open type. Two specific length-to-depth ratios were studied while varying such parameters as the offset ratio and the aft ramp angle. Measurements included both conventional visualizations and wall static pressures from upstream of and within the cavity. Also included in the report is a detailed calibration of a new facility nozzle for AFRL/PRSS Test Cell 19.

The new facility nozzle was found to operate cleanly with relatively small disturbances to the freestream flow from undesired waves. The behavior of the nozzle was independent of operating conditions and the probe results showed a spatially uniform core flow with a well-behaved boundary layer on the lower wall of the test section. Nozzle pressure data were spanwise symmetric and collapsed for a wide range of stagnation pressures.

The seven cavity geometries were tested in conjunction with the new facility nozzle and their characteristics were documented using schlieren and shadowgraph flow visualization techniques. The wall static pressure distribution was documented both along the spanwise symmetry plane and off the symmetry plane to assess the two-dimensionality of the flowfield. Results indicate that the aft ramp angle plays a strong role in determining the character of the shear layer which spans the length of the cavity. For rectangular cavities (i.e., aft ramp angle = 90°), a compression wave forms as the flow separates from the upstream corner of the cavity. Thus, the pressure on the upstream face increases above the freestream value. In these cases, the recompression which occurs at the aft wall is very sharp with strong pressure gradients at the axial location corresponding to the aft wall. These cases are also visibly unsteady as evidenced by the flow visualizations and the periodic waves which interact with the main separation and recompression shocks. Reductions in the aft ramp angle below 90° yield more stable, two-dimensional flowfields. However, the character of the separation wave changes from compressive (in the $\theta = 90^\circ$ and 30° cases) to expansive (in the $\theta = 16^\circ$ case). As such, the pressure on the

upstream face of the cavity steadily decreases as the ramp angle decreases. The shear layer tends to dip into the cavity for these cases and the recompression occurs more gradually as the shear layer reattaches to the cavity aft wall.

Changes in the offset ratio cause more drastic changes to the cavity flowfield. First, the separation wave is observed to be relatively strong and expansive in nature. The upstream face of the cavity experiences a much lower pressure in these cases than in any of the configuration where offset ratio is unity. The shear layer dips much further into the cavity. The aft ramp angle has less influence on the overall cavity performance in these cases: no appreciable change in the pressure at the upstream face occurred as the ramp angle was decreased from 90° to 16° . Of course, the recompression wave structure changed slightly in response to the angle aft ramp.

Future work on these configurations will involve their characterization in terms of entrainment rate, residence time, and velocity field. Such measurements are currently underway. Acoustic pressure levels will be characterized to lend credence to the observed stabilizing effects of the aft ramp angle. Additionally, direct comparisons to CFD will be made using the present and future data sets. Finally, plans for small-scale combustion tests to be conducted using these geometries to verify their performance in supersonic reacting flows are presently underway.

Tables

Table 4.1 Mach 3 Nozzle Contour Coordinates

x	y	x	y	x	y	x	y
0.0000	0.0000	4.3000	0.3888	8.6000	1.5551	12.1500	2.4091
0.1000	0.0002	4.4000	0.4071	8.7000	1.5915	12.2000	2.3978
0.2000	0.0008	4.5000	0.4258	8.8000	1.6283	12.2500	2.3853
0.3000	0.0019	4.6000	0.4449	8.9000	1.6655	12.3000	2.3722
0.4000	0.0034	4.7000	0.4645	9.0000	1.7031	12.3500	2.3586
0.5000	0.0053	4.8000	0.4845	9.1000	1.7412	12.4000	2.3434
0.6000	0.0076	4.9000	0.5048	9.2000	1.7797	12.4500	2.3276
0.7000	0.0103	5.0000	0.5257	9.3000	1.8186	12.5000	2.3113
0.8000	0.0135	5.1000	0.5469	9.4000	1.8579	12.5500	2.2938
0.9000	0.0170	5.2000	0.5686	9.5000	1.8976	12.6000	2.2756
1.0000	0.0210	5.3000	0.5906	9.6000	1.9378	12.6500	2.2568
1.1000	0.0254	5.4000	0.6131	9.7000	1.9784	12.7000	2.2365
1.2000	0.0303	5.5000	0.6361	9.8000	2.0194	12.7500	2.2161
1.3000	0.0355	5.6000	0.6594	9.9000	2.0608	12.8000	2.1952
1.4000	0.0412	5.7000	0.6831	10.0000	2.1026	12.8500	2.1747
1.5000	0.0473	5.8000	0.7073	10.1000	2.1449	12.9000	2.1545
1.6000	0.0538	5.9000	0.7319	10.2000	2.1876	12.9500	2.1344
1.7000	0.0608	6.0000	0.7569	10.3000	2.2307	13.0000	2.1142
1.8000	0.0681	6.1000	0.7824	10.3110	2.2352	13.0500	2.0946
1.9000	0.0759	6.2000	0.8083	10.4000	2.2723	13.1000	2.0751
2.0000	0.0841	6.3000	0.8345	10.5000	2.3098	13.1500	2.0555
2.1000	0.0927	6.4000	0.8612	10.6000	2.3433	13.2000	2.0365
2.2000	0.1018	6.5000	0.8884	10.7000	2.3730	13.2500	2.0172
2.3000	0.1112	6.6000	0.9159	10.8000	2.3989	13.3000	1.9985
2.4000	0.1211	6.7000	0.9439	10.9000	2.4212	13.3500	1.9799
2.5000	0.1314	6.8000	0.9723	11.0000	2.4399	13.4000	1.9614
2.6000	0.1421	6.9000	1.0011	11.1000	2.4551	13.4500	1.9429
2.7000	0.1533	7.0000	1.0303	11.2000	2.4669	13.5000	1.9249
2.8000	0.1649	7.1000	1.0599	11.3000	2.4753	13.5500	1.9068
2.9000	0.1768	7.2000	1.0900	11.4000	2.4803	13.6000	1.8889
3.0000	0.1892	7.3000	1.1205	11.5000	2.4820	13.6500	1.8714
3.1000	0.2021	7.4000	1.1514	11.5500	2.4814	13.7000	1.8539
3.2000	0.2153	7.5000	1.1827	11.6000	2.4799	13.7500	1.8364
3.3000	0.2290	7.6000	1.2145	11.6500	2.4778	13.8000	1.8194
3.4000	0.2431	7.7000	1.2467	11.7000	2.4747	13.8500	1.8025
3.5000	0.2576	7.8000	1.2792	11.7500	2.4708	13.9000	1.7859
3.6000	0.2725	7.9000	1.3123	11.8000	2.4661	13.9500	1.7695
3.7000	0.2879	8.0000	1.3457	11.8500	2.4603	14.0000	1.7531
3.8000	0.3036	8.1000	1.3795	11.9000	2.4531	14.0500	1.7368
3.9000	0.3198	8.2000	1.4138	11.9500	2.4460	14.1000	1.7204
4.0000	0.3364	8.3000	1.4485	12.0000	2.4387	14.1500	1.7045
4.1000	0.3535	8.4000	1.4836	12.0500	2.4294	14.2000	1.6889
4.2000	0.3709	8.5000	1.5192	12.1000	2.4200	14.2500	1.6733

x	y	x	y	x	y	x	y
14.3000	1.6577	16.6500	1.0824	19.0000	0.7380	21.3500	0.5567
14.3500	1.6421	16.7000	1.0729	19.0500	0.7327	21.4000	0.5543
14.4000	1.6271	16.7500	1.0637	19.1000	0.7274	21.4500	0.5521
14.4500	1.6122	16.8000	1.0545	19.1500	0.7221	21.5000	0.5498
14.5000	1.5974	16.8500	1.0453	19.2000	0.7168	21.5500	0.5476
14.5500	1.5825	16.9000	1.0363	19.2500	0.7118	21.6000	0.5453
14.6000	1.5676	16.9500	1.0274	19.3000	0.7068	21.6500	0.5431
14.6500	1.5535	17.0000	1.0186	19.3500	0.7019	21.7000	0.5410
14.7000	1.5393	17.0500	1.0097	19.4000	0.6970	21.7500	0.5391
14.7500	1.5252	17.1000	1.0011	19.4500	0.6921	21.8000	0.5372
14.8000	1.5110	17.1500	0.9927	19.5000	0.6874	21.8500	0.5352
14.8500	1.4969	17.2000	0.9843	19.5500	0.6828	21.9000	0.5333
14.9000	1.4834	17.2500	0.9759	19.6000	0.6782	21.9500	0.5314
14.9500	1.4699	17.3000	0.9677	19.6500	0.6735	22.0000	0.5296
15.0000	1.4564	17.3500	0.9596	19.7000	0.6689	22.0500	0.5280
15.0500	1.4431	17.4000	0.9515	19.7500	0.6646	22.1000	0.5265
15.1000	1.4300	17.4500	0.9434	19.8000	0.6603	22.1500	0.5249
15.1500	1.4170	17.5000	0.9355	19.8500	0.6561	22.2000	0.5233
15.2000	1.4039	17.5500	0.9278	19.9000	0.6518	22.2500	0.5218
15.2500	1.3912	17.6000	0.9201	19.9500	0.6475	22.3000	0.5202
15.3000	1.3787	17.6500	0.9124	20.0000	0.6435	22.3500	0.5189
15.3500	1.3661	17.7000	0.9049	20.0500	0.6396	22.4000	0.5176
15.4000	1.3535	17.7500	0.8976	20.1000	0.6357	22.4500	0.5164
15.4500	1.3414	17.8000	0.8902	20.1500	0.6318	22.5000	0.5152
15.5000	1.3293	17.8500	0.8829	20.2000	0.6279	22.5500	0.5140
15.5500	1.3172	17.9000	0.8757	20.2500	0.6241	22.6000	0.5128
15.6000	1.3052	17.9500	0.8687	20.3000	0.6206	22.6500	0.5115
15.6500	1.2935	18.0000	0.8616	20.3500	0.6170	22.7000	0.5106
15.7000	1.2819	18.0500	0.8546	20.4000	0.6134	22.7500	0.5097
15.7500	1.2702	18.1000	0.8477	20.4500	0.6098	22.8000	0.5088
15.8000	1.2588	18.1500	0.8411	20.5000	0.6062	22.8500	0.5079
15.8500	1.2476	18.2000	0.8344	20.5500	0.6029	22.9000	0.5070
15.9000	1.2364	18.2500	0.8278	20.6000	0.5996	22.9500	0.5061
15.9500	1.2252	18.3000	0.8211	20.6500	0.5964	23.0000	0.5053
16.0000	1.2145	18.3500	0.8148	20.7000	0.5931	23.0500	0.5047
16.0500	1.2037	18.4000	0.8084	20.7500	0.5899	23.1000	0.5041
16.1000	1.1930	18.4500	0.8021	20.8000	0.5867	23.1500	0.5036
16.1500	1.1824	18.5000	0.7958	20.8500	0.5838	23.2000	0.5030
16.2000	1.1720	18.5500	0.7896	20.9000	0.5809	23.2500	0.5024
16.2500	1.1616	18.6000	0.7837	20.9500	0.5780	23.3000	0.5019
16.3000	1.1513	18.6500	0.7777	21.0000	0.5751	23.3500	0.5013
16.3500	1.1411	18.7000	0.7718	21.0500	0.5721	23.4000	0.5009
16.4000	1.1311	18.7500	0.7659	21.1000	0.5694	23.4500	0.5005
16.4500	1.1212	18.8000	0.7603	21.1500	0.5669	23.5000	0.5003
16.5000	1.1112	18.8500	0.7547	21.2000	0.5643	23.5500	0.5000
16.5500	1.1016	18.9000	0.7490	21.2500	0.5618	23.6000	0.5000
16.6000	1.0920	18.9500	0.7434	21.3000	0.5592	24.0000	0.5000

Table 5.1 Cavity Geometry Specifications

Name	L/D	Offset Ratio (OR)	Ramp Angle (θ)
LD3-O1	3	1	90°
LD3-O1-16	3	1	16°
LD3-O1-30	3	1	30°
LD3-O2	3	2	90°
LD3-O2-16	3	2	16°
LD5-O1	5	1	90°
LD5-O1-16	5	1	16°

Table 5.2 Cavity Instrumentation Locations

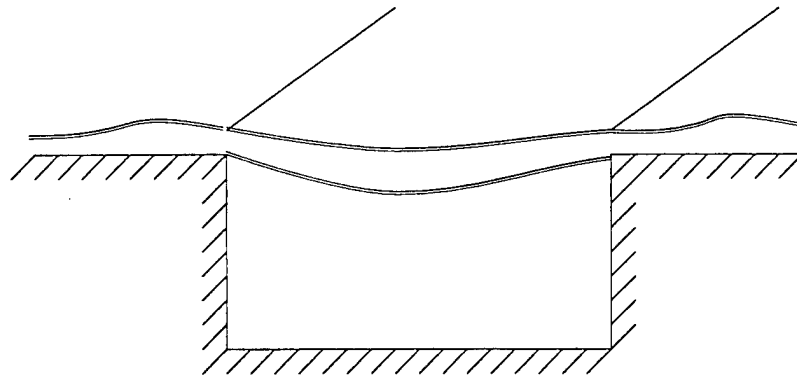
Name	x (inches)	y (inches)	z (inches)	Description
PR0103	-0.396	0.000	0.000	Forward ramp
PR0203	-1.021	0.000	0.000	Forward ramp
PR0303	-1.646	0.000	0.000	Forward ramp
PF0101	0.000	-0.162	0.375	Backstep
PF0102	0.000	-0.162	0.188	Backstep
PF0104	0.000	-0.162	-0.188	Backstep
PF0105	0.000	-0.162	-0.375	Backstep
PA0103	0.094	-0.350	0.000	LD3-O1
PA0201	0.219	-0.350	0.375	LD3-O1
PA0202	0.219	-0.350	0.188	LD3-O1
PA0204	0.219	-0.350	-0.188	LD3-O1
PA0205	0.219	-0.350	-0.375	LD3-O1
PA0303	0.344	-0.350	0.000	LD3-O1
PA0403	0.469	-0.350	0.000	LD3-O1
PA0503	0.594	-0.350	0.000	LD3-O1
PA0601	0.719	-0.350	0.375	LD3-O1
PA0602	0.719	-0.350	0.188	LD3-O1
PA0603	0.719	-0.350	0.000	LD3-O1
PA0604	0.719	-0.350	-0.188	LD3-O1
PA0605	0.719	-0.350	-0.375	LD3-O1
PA0703	0.844	-0.350	0.000	LD3-O1
PA0901	1.050	-0.162	0.375	LD3-O1
PA0902	1.050	-0.162	0.188	LD3-O1
PA0904	1.050	-0.162	-0.188	LD3-O1
PA0905	1.050	-0.162	-0.375	LD3-O1
PA0103	0.094	-0.350	0.000	LD3-O1-16
PA0201	0.219	-0.350	0.375	LD3-O1-16
PA0202	0.219	-0.350	0.188	LD3-O1-16
PA0204	0.219	-0.350	-0.188	LD3-O1-16
PA0205	0.219	-0.350	-0.375	LD3-O1-16
PA0303	0.344	-0.350	0.000	LD3-O1-16
PA0401	0.560	-0.316	0.375	LD3-O1-16
PA0402	0.560	-0.316	0.188	LD3-O1-16

PA0404	0.560	-0.316	-0.188	LD3-O1-16
PA0405	0.560	-0.316	-0.375	LD3-O1-16
PA0503	0.741	-0.264	0.000	LD3-O1-16
PA0603	0.922	-0.212	0.000	LD3-O1-16
PA0701	1.102	-0.160	0.375	LD3-O1-16
PA0702	1.102	-0.160	0.188	LD3-O1-16
PA0703	1.102	-0.160	0.000	LD3-O1-16
PA0704	1.102	-0.160	-0.188	LD3-O1-16
PA0705	1.102	-0.160	-0.375	LD3-O1-16
PA0803	1.283	-0.108	0.000	LD3-O1-16
PA0901	1.464	-0.056	0.375	LD3-O1-16
PA0902	1.464	-0.056	0.188	LD3-O1-16
PA0904	1.464	-0.056	-0.188	LD3-O1-16
PA0905	1.464	-0.056	-0.375	LD3-O1-16
PA0103	0.094	-0.350	0.000	LD3-O1-30
PA0201	0.219	-0.350	0.375	LD3-O1-30
PA0202	0.219	-0.350	0.188	LD3-O1-30
PA0204	0.219	-0.350	-0.188	LD3-O1-30
PA0205	0.219	-0.350	-0.375	LD3-O1-30
PA0303	0.344	-0.350	0.000	LD3-O1-30
PA0403	0.469	-0.350	0.000	LD3-O1-30
PA0503	0.594	-0.350	0.000	LD3-O1-30
PA0601	0.855	-0.288	0.375	LD3-O1-30
PA0602	0.855	-0.288	0.188	LD3-O1-30
PA0604	0.855	-0.288	-0.188	LD3-O1-30
PA0605	0.855	-0.288	-0.375	LD3-O1-30
PA0703	0.964	-0.225	0.000	LD3-O1-30
PA0803	1.072	-0.162	0.000	LD3-O1-30
PA0903	1.180	-0.100	0.000	LD3-O1-30
PA1001	1.288	-0.038	0.375	LD3-O1-30
PA1002	1.288	-0.038	0.188	LD3-O1-30
PA1004	1.288	-0.038	-0.188	LD3-O1-30
PA1005	1.288	-0.038	-0.375	LD3-O1-30
PA0103	0.094	-0.350	0.000	LD3-O2
PA0201	0.219	-0.350	0.375	LD3-O2
PA0202	0.219	-0.350	0.188	LD3-O2
PA0204	0.219	-0.350	-0.188	LD3-O2
PA0205	0.219	-0.350	-0.375	LD3-O2
PA0303	0.344	-0.350	0.000	LD3-O2
PA0403	0.469	-0.350	0.000	LD3-O2
PA0503	0.594	-0.350	0.000	LD3-O2
PA0601	0.719	-0.350	0.375	LD3-O2
PA0602	0.719	-0.350	0.188	LD3-O2
PA0603	0.719	-0.350	0.000	LD3-O2
PA0604	0.719	-0.350	-0.188	LD3-O2
PA0605	0.719	-0.350	-0.375	LD3-O2
PA0703	0.844	-0.350	0.000	LD3-O2
PA0803	0.969	-0.350	0.000	LD3-O2
PA0901	1.050	-0.162	0.375	LD3-O2

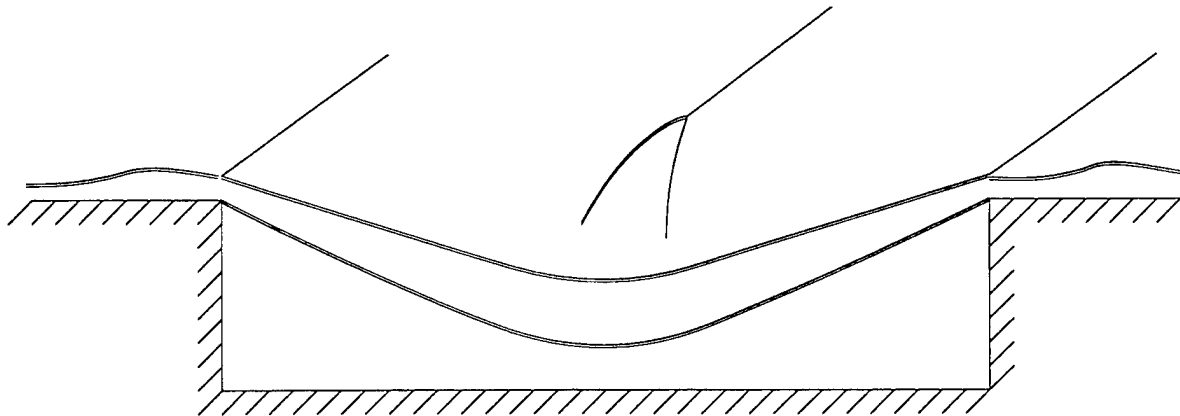
PA0902	1.050	-0.162	0.188	LD3-O2
PA0903	1.050	-0.162	0.000	LD3-O2
PA0904	1.050	-0.162	-0.188	LD3-O2
PA0905	1.050	-0.162	-0.375	LD3-O2
PA0103	0.094	-0.350	0.000	LD3-O2-16
PA0201	0.219	-0.350	0.375	LD3-O2-16
PA0202	0.219	-0.350	0.188	LD3-O2-16
PA0204	0.219	-0.350	-0.188	LD3-O2-16
PA0205	0.219	-0.350	-0.375	LD3-O2-16
PA0303	0.344	-0.350	0.000	LD3-O2-16
PA0403	0.469	-0.350	0.000	LD3-O2-16
PA0503	0.594	-0.350	0.000	LD3-O2-16
PA0601	0.865	-0.316	0.375	LD3-O2-16
PA0602	0.865	-0.316	0.188	LD3-O2-16
PA0604	0.865	-0.316	-0.188	LD3-O2-16
PA0605	0.865	-0.316	-0.375	LD3-O2-16
PA0703	1.046	-0.264	0.000	LD3-O2-16
PA0801	1.247	-0.212	0.375	LD3-O2-16
PA0802	1.247	-0.212	0.188	LD3-O2-16
PA0804	1.247	-0.212	-0.188	LD3-O2-16
PA0805	1.247	-0.212	-0.375	LD3-O2-16
PA0103	0.094	-0.350	0.000	LD5-O1
PA0201	0.219	-0.350	0.375	LD5-O1
PA0202	0.219	-0.350	0.188	LD5-O1
PA0204	0.219	-0.350	-0.188	LD5-O1
PA0205	0.219	-0.350	-0.375	LD5-O1
PA0303	0.344	-0.350	0.000	LD5-O1
PA0403	0.469	-0.350	0.000	LD5-O1
PA0503	0.594	-0.350	0.000	LD5-O1
PA0603	0.719	-0.350	0.000	LD5-O1
PA0703	0.844	-0.350	0.000	LD5-O1
PA0803	0.969	-0.350	0.000	LD5-O1
PA0903	1.094	-0.350	0.000	LD5-O1
PA1003	1.219	-0.350	0.000	LD5-O1
PA1101	1.344	-0.350	0.375	LD5-O1
PA1102	1.344	-0.350	0.188	LD5-O1
PA1103	1.344	-0.350	0.000	LD5-O1
PA1104	1.344	-0.350	-0.188	LD5-O1
PA1105	1.344	-0.350	-0.375	LD5-O1
PA1203	1.469	-0.350	0.000	LD5-O1
PA1401	1.750	-0.162	0.375	LD5-O1
PA1402	1.750	-0.162	0.188	LD5-O1
PA1404	1.750	-0.162	-0.188	LD5-O1
PA1405	1.750	-0.162	-0.375	LD5-O1
PA0103	0.094	-0.350	0.000	LD5-O1-16
PA0201	0.219	-0.350	0.375	LD5-O1-16
PA0202	0.219	-0.350	0.188	LD5-O1-16
PA0204	0.219	-0.350	-0.188	LD5-O1-16
PA0205	0.219	-0.350	-0.375	LD5-O1-16

PA0303	0.344	-0.350	0.000	LD5-O1-16
PA0403	0.469	-0.350	0.000	LD5-O1-16
PA0503	0.594	-0.350	0.000	LD5-O1-16
PA0603	0.719	-0.350	0.000	LD5-O1-16
PA0703	0.844	-0.350	0.000	LD5-O1-16
PA0803	0.969	-0.350	0.000	LD5-O1-16
PA0901	1.260	-0.316	0.375	LD5-O1-16
PA0902	1.260	-0.316	0.188	LD5-O1-16
PA0904	1.260	-0.316	-0.188	LD5-O1-16
PA0905	1.260	-0.316	-0.375	LD5-O1-16
PA1003	1.440	-0.264	0.000	LD5-O1-16
PA1103	1.621	-0.212	0.000	LD5-O1-16
PA1203	1.801	-0.160	0.000	LD5-O1-16
PA1303	1.981	-0.108	0.000	LD5-O1-16
PA1401	2.161	-0.056	0.375	LD5-O1-16
PA1402	2.161	-0.056	0.188	LD5-O1-16
PA1404	2.161	-0.056	-0.188	LD5-O1-16
PA1405	2.161	-0.056	-0.375	LD5-O1-16

Figures



(a) Open Cavity Flow ($L/D < 10$)



(b) Closed Cavity Flow ($L/D > 10$)

Figure 2.1 Character of Cavity Flows (a) Open Cavity Flow, (b) Closed Cavity Flow

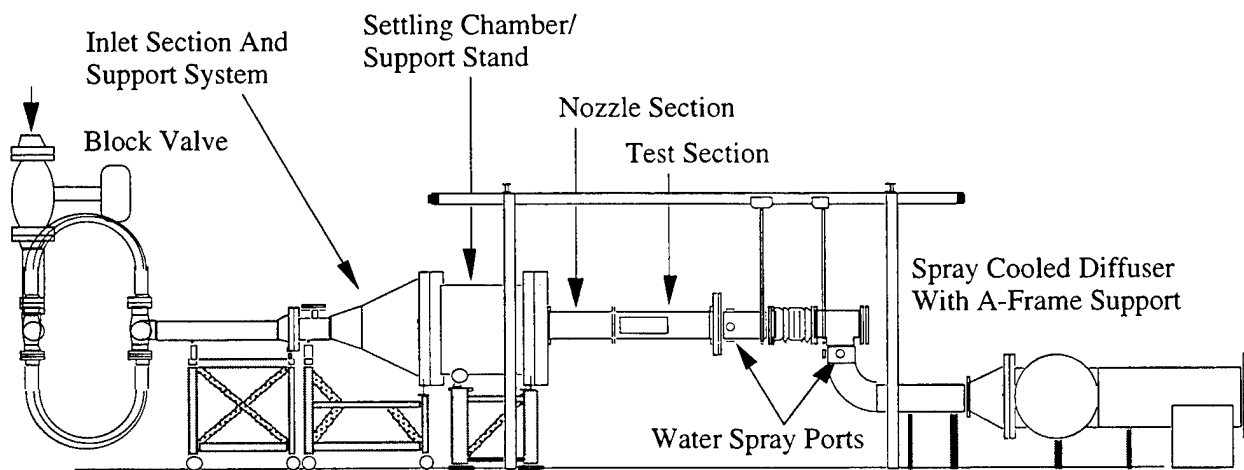


Figure 3.1 Room 19 Facility Schematic

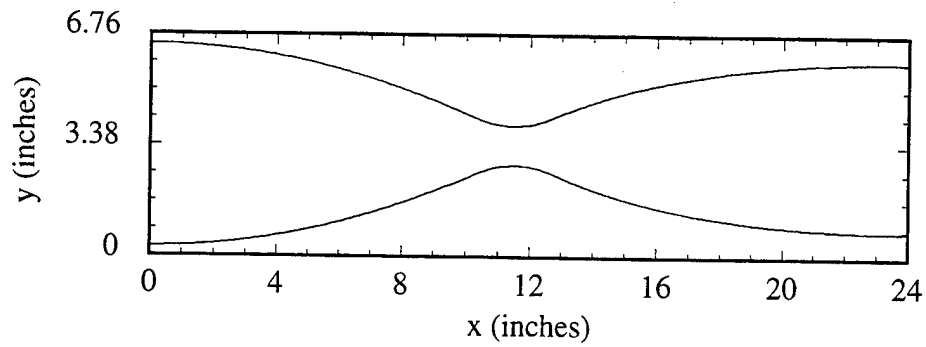


Figure 4.1 Mach 3 Nozzle Contour

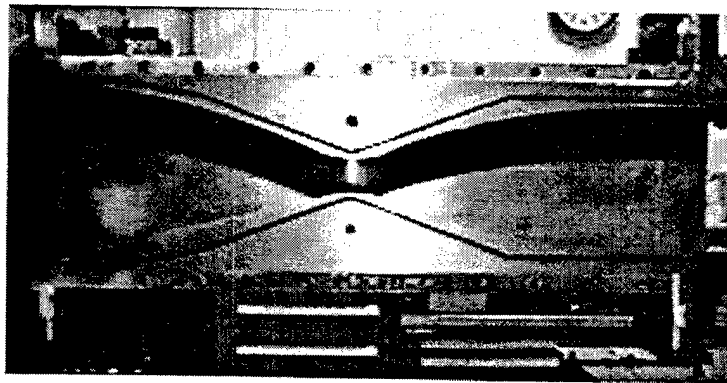
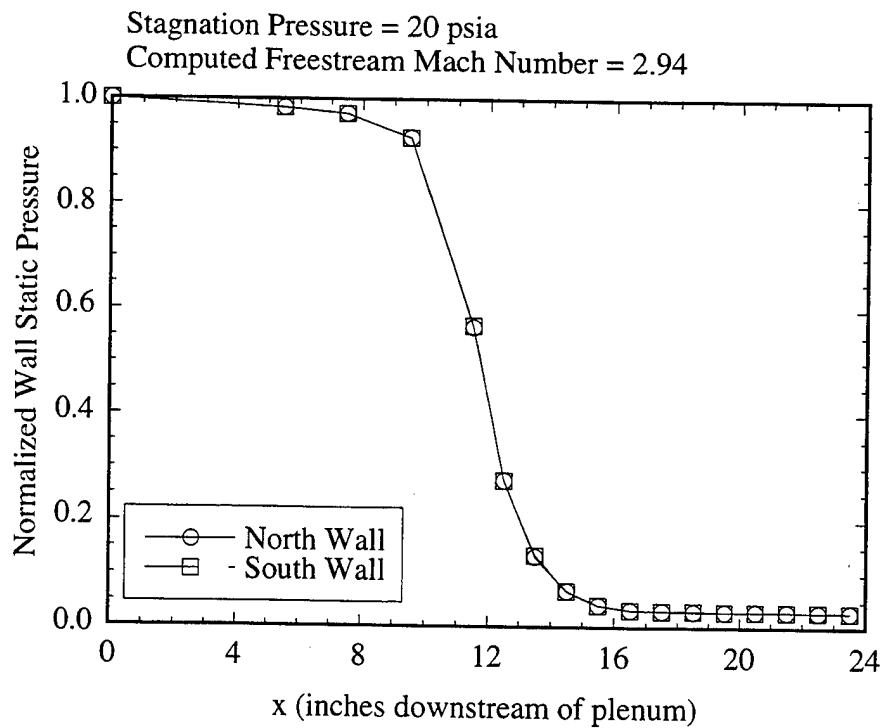
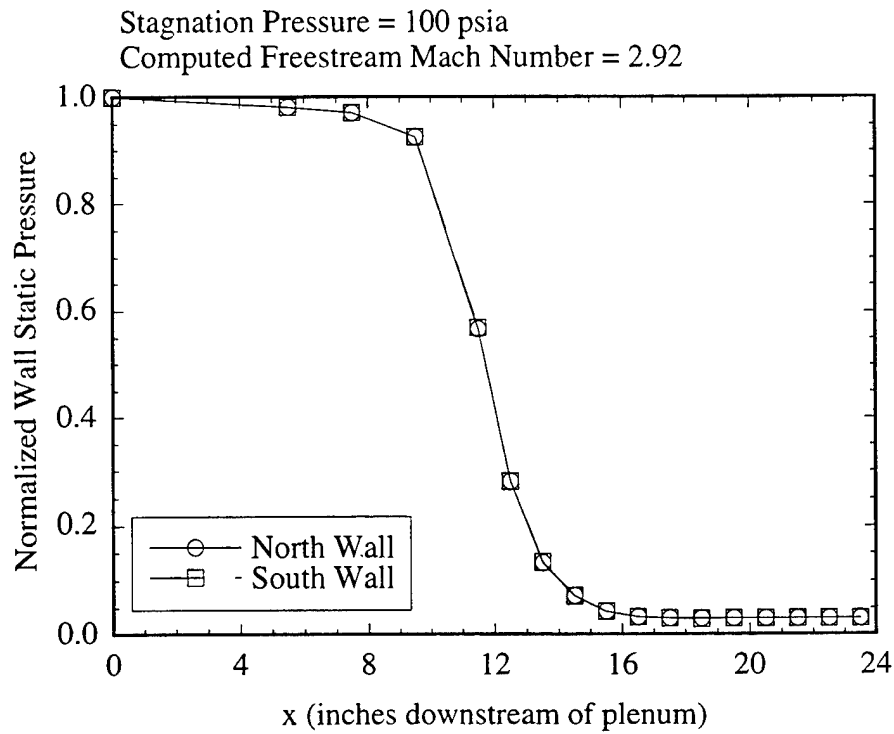


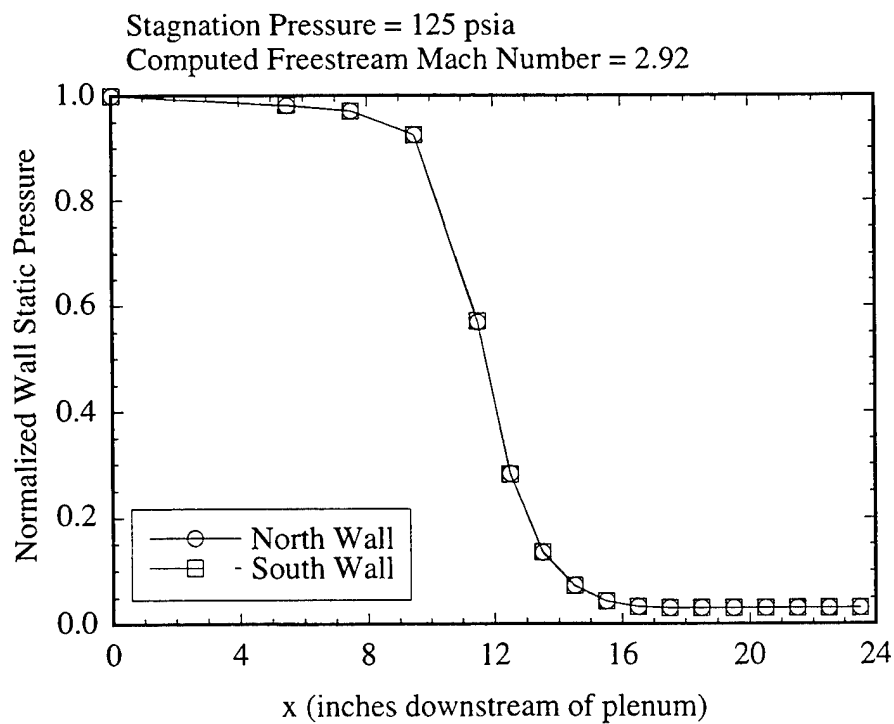
Figure 4.2 Mach 3 Nozzle Installed in Room 19



(a) Stagnation Pressure = 20 psia

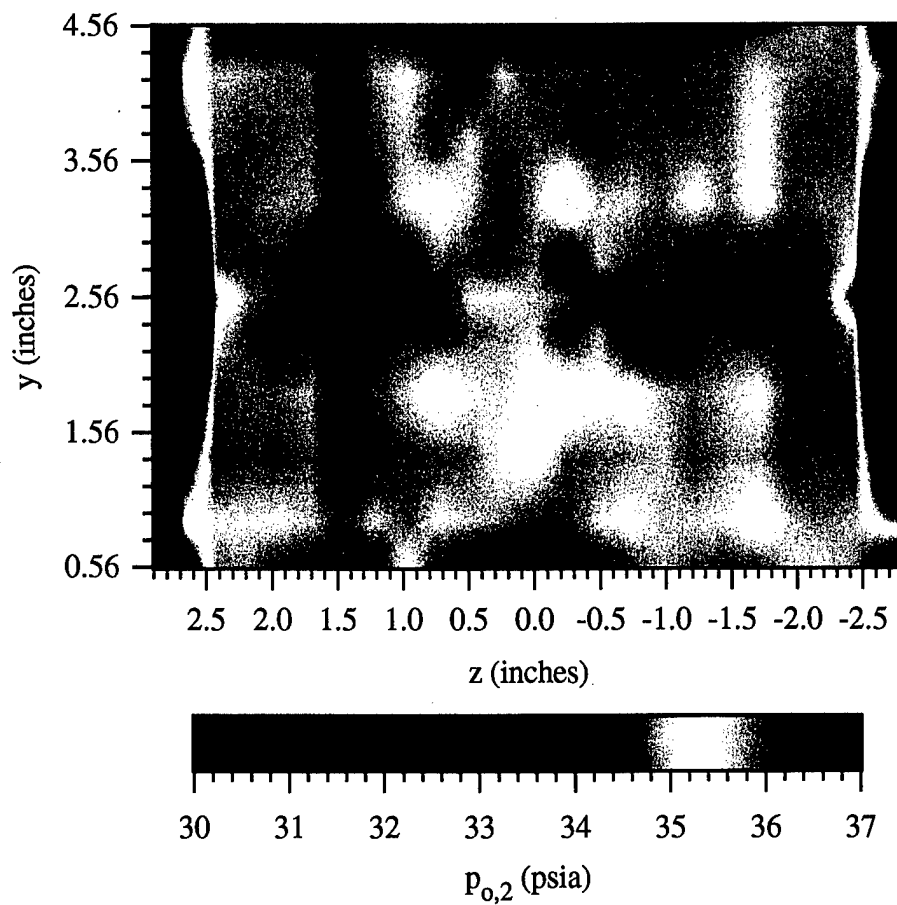


(b) Stagnation Pressure = 100 psia

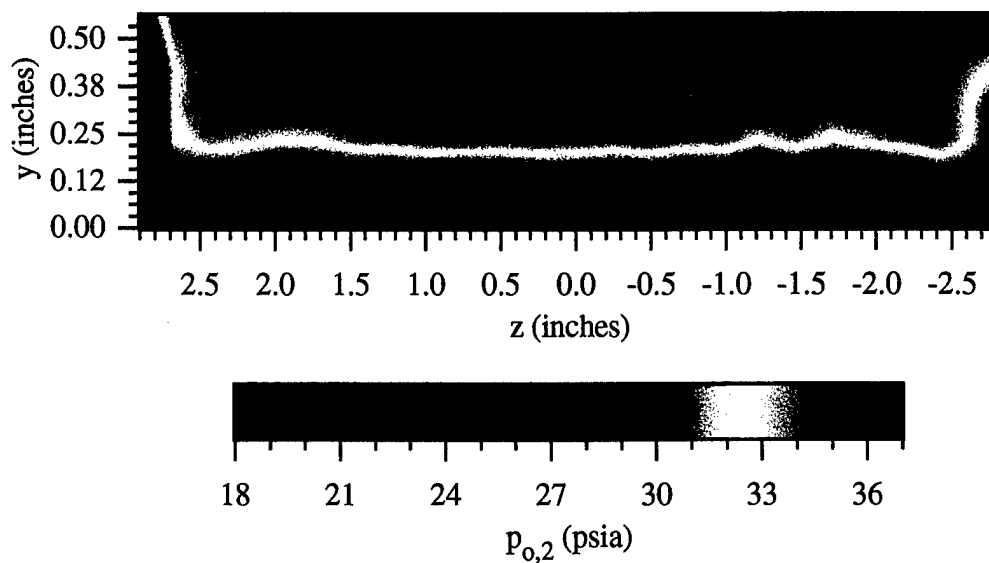


(c) Stagnation Pressure = 125 psia

Figure 4.3 Mach 3 Nozzle Normalized Sidewall Pressure Distributions (a) Stagnation Pressure = 20 psia, (b) Stagnation Pressure = 100 psia, (c) Stagnation Pressure = 125 psia



(a) Core Region



(b) Near-Wall Region

Figure 4.4 Pitot Pressure Distributions at $x = 13.5$ " Downstream of Nozzle Exit (Stagnation Pressure = 100 psia) (a) Core Region, (b) Near-Wall Region

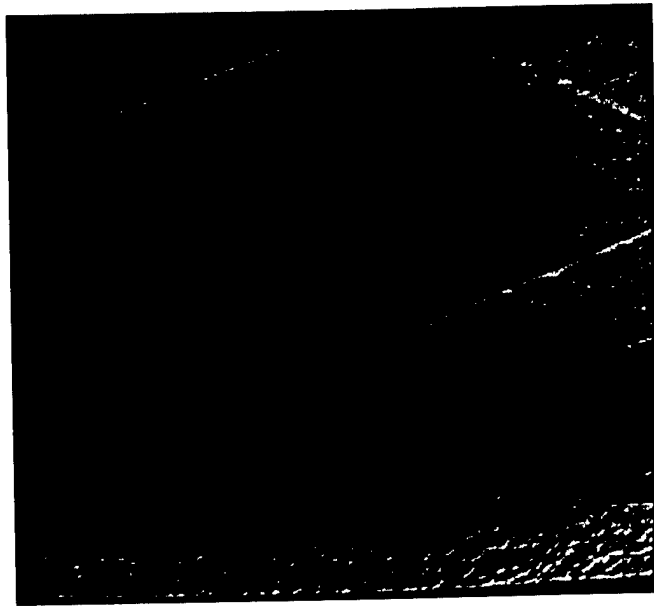
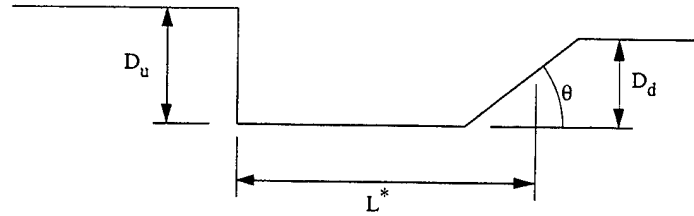


Figure 4.5 Shadowgraph Photo from Clean Test Section (Flow is Left to Right)

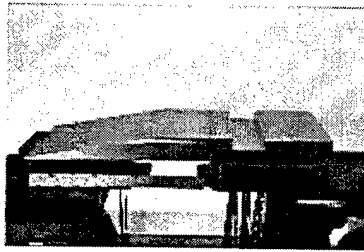


Figure 4.6 Shadowgraph Photo of Circular Jet in Crossflow



*Cavity length (L) = length of rectangular cavity or distance from leading edge to $0.5 \cdot (D_d / \tan(\theta))$ for angled ramp. Offset ratio (OR) is the ratio of D_u to D_d .

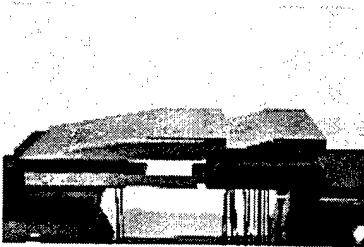
Figure 5.1 Cavity Geometry Schematic



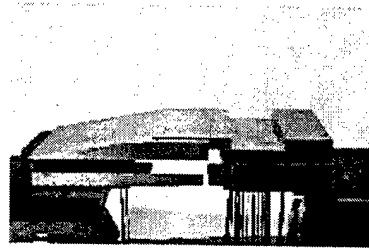
(a) LD3-O1



(e) LD3-O2-16



(b) LD3-O1-16



(f) LD5-O1



(c) LD3-O1-30



(g) LD5-O1-16



(d) LD3-O2

Figure 5.2 Photographs of Cavity Models (a) LD3-O1, (b) LD3-O1-16, (c) LD3-O1-30, (d) LD3-O2, (e) LD3-O2-16, (f) LD5-O1, (g) LD5-O1-16

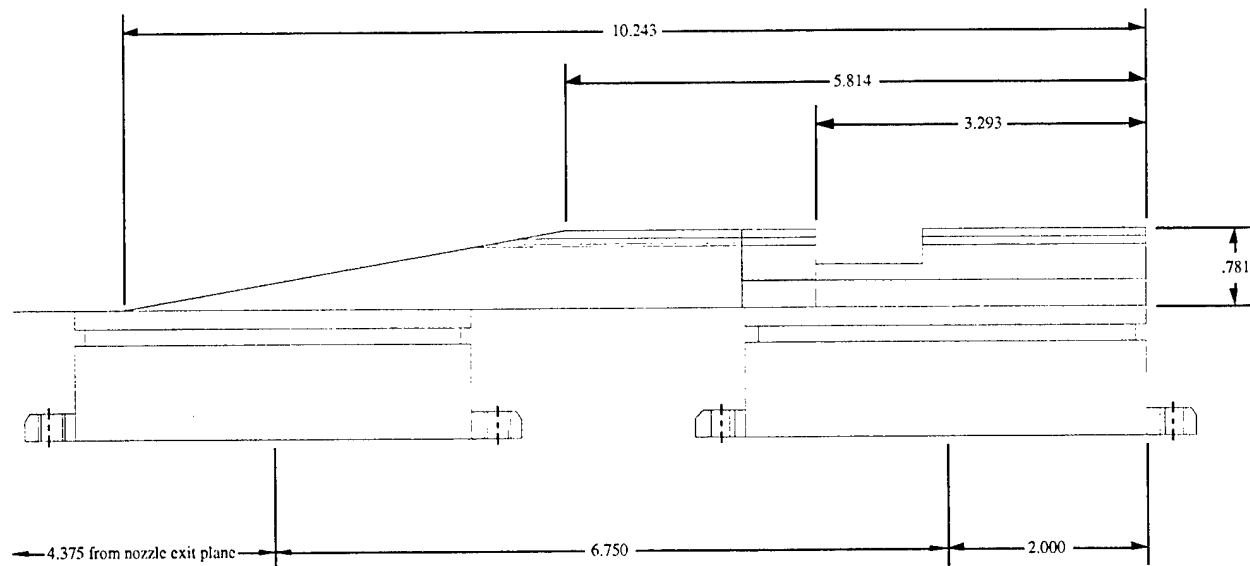
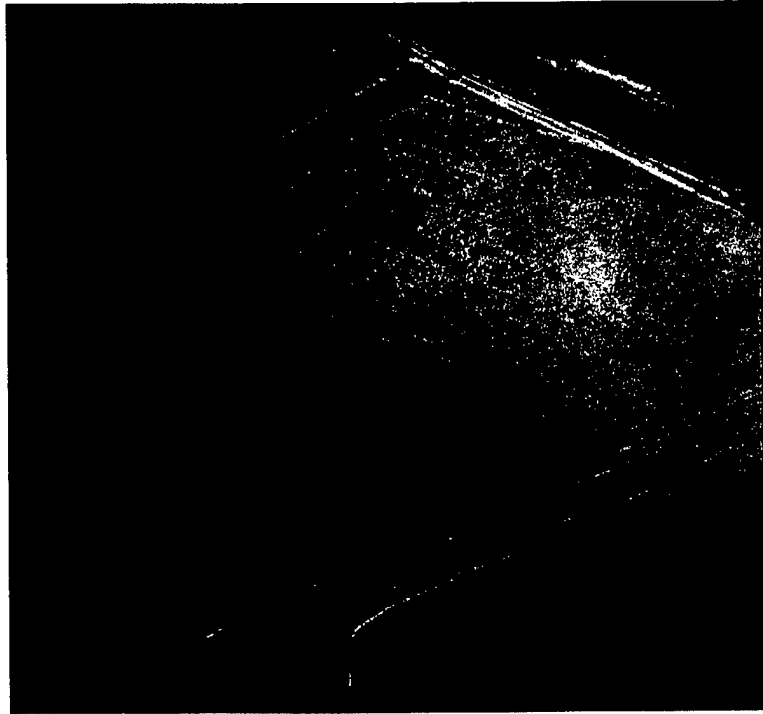
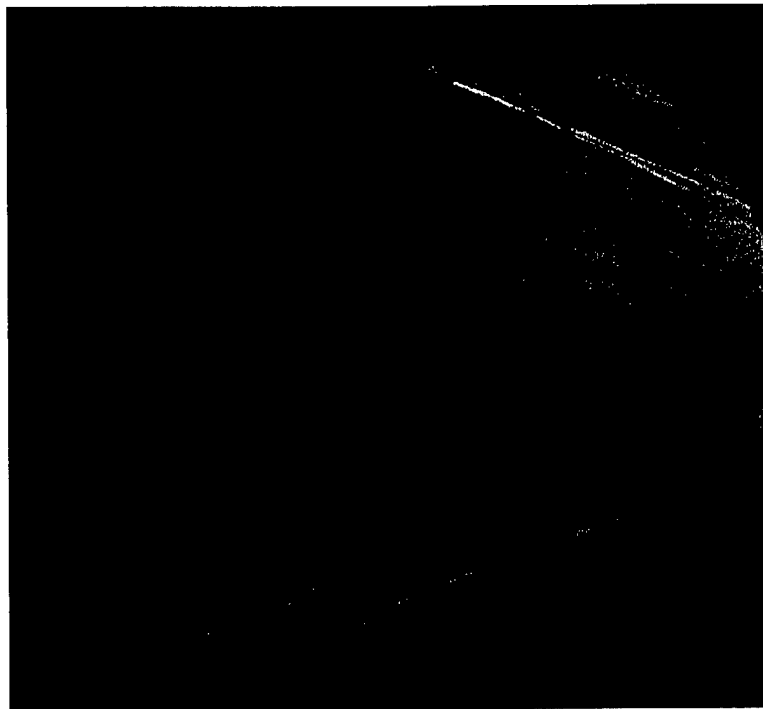


Figure 5.3 Representative Cavity Assembly Drawing (LD3-O1)



(a) Shadowgraph Photo

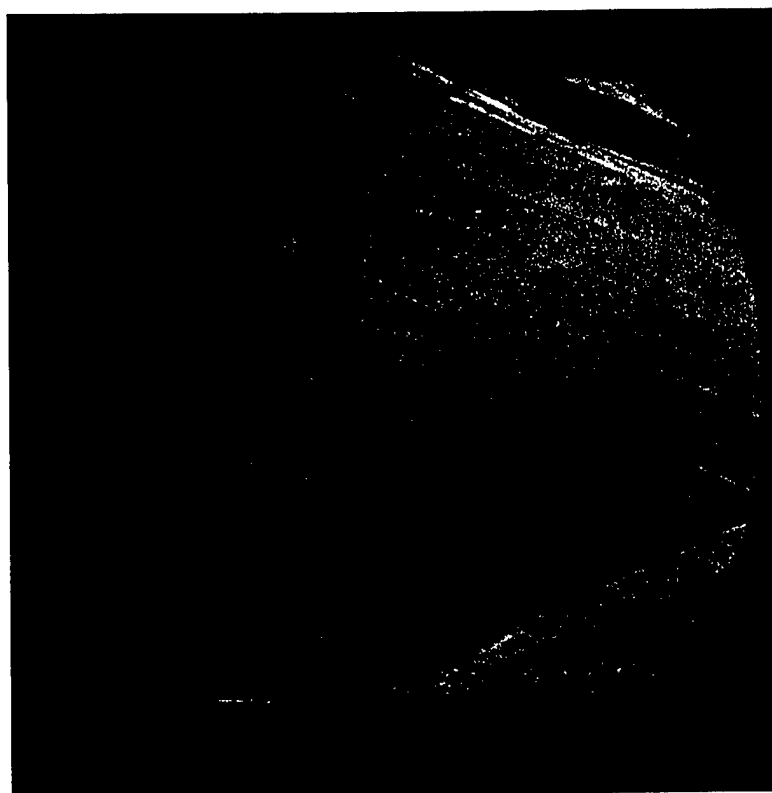


(b) Schlieren Photo

Figure 6.1 Visualizations of LD3-O1 (a) Shadowgraph Photo, (b) Schlieren Photo

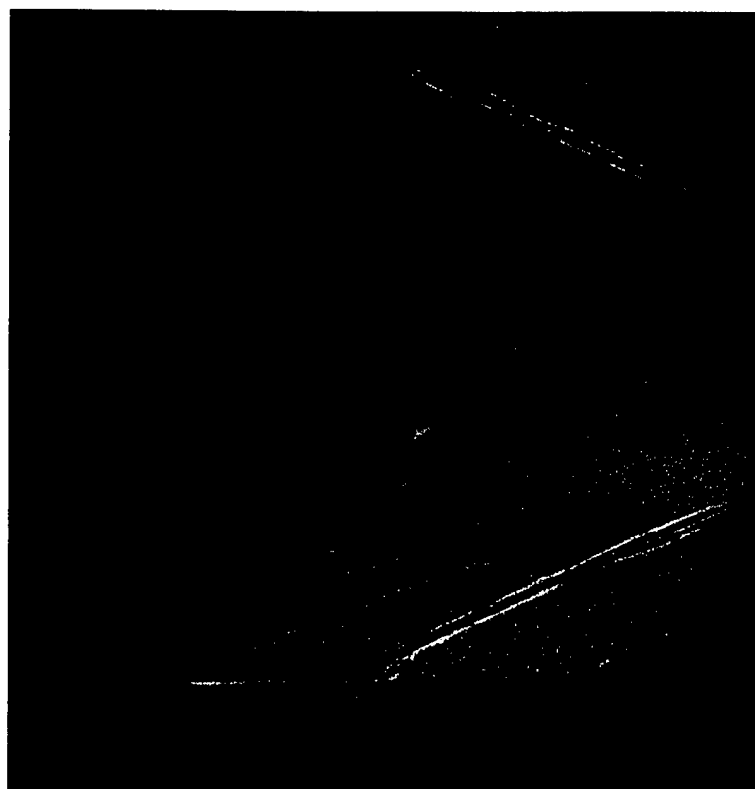


(a) Shadowgraph Photo

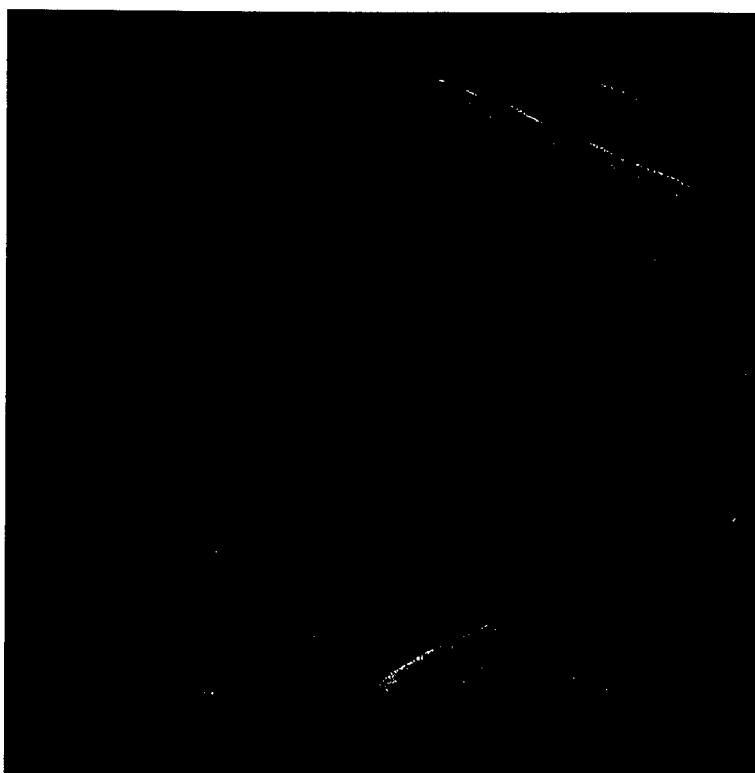


(b) Schlieren Photo

Figure 6.2 Visualizations of LD3-O1-16 (a) Shadowgraph Photo, (b) Schlieren Photo

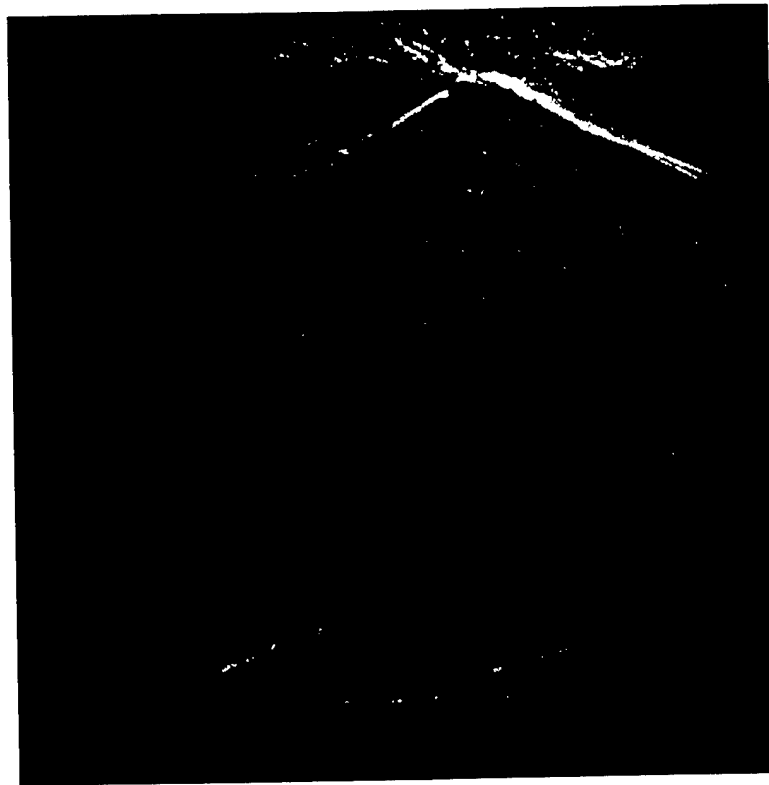


(a) Shadowgraph Photo

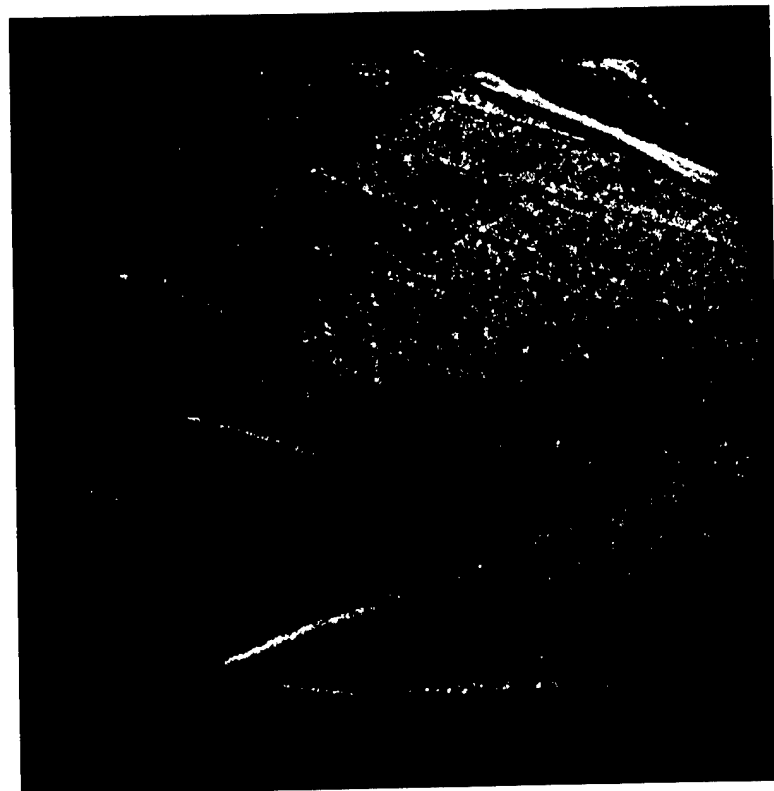


(b) Schlieren Photo

Figure 6.3 Visualizations of LD3-O1-30 (a) Shadowgraph Photo, (b) Schlieren Photo



(a) Shadowgraph Photo

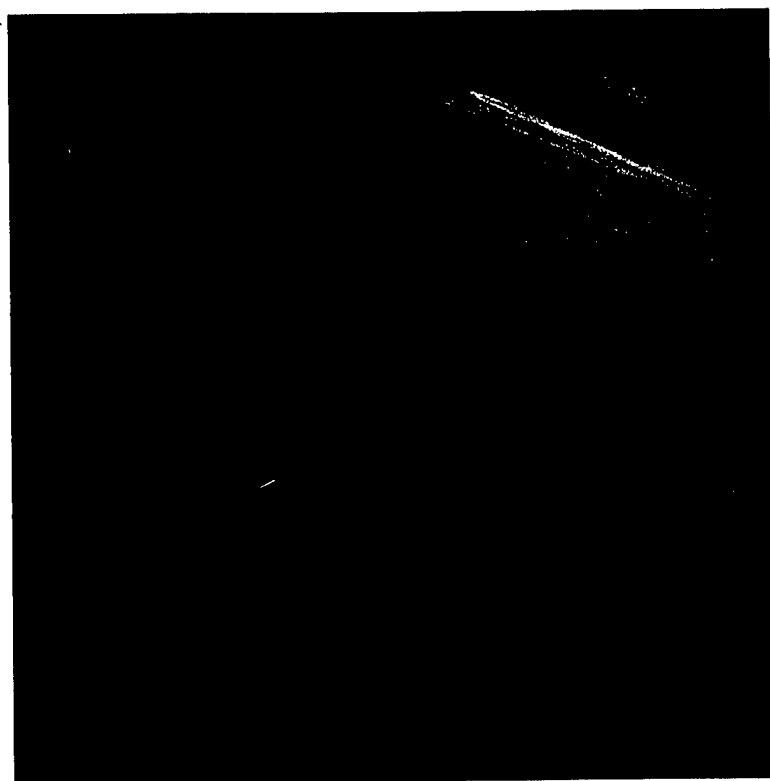


(b) Schlieren Photo

Figure 6.4 Visualizations of LD3-O2 (a) Shadowgraph Photo, (b) Schlieren Photo

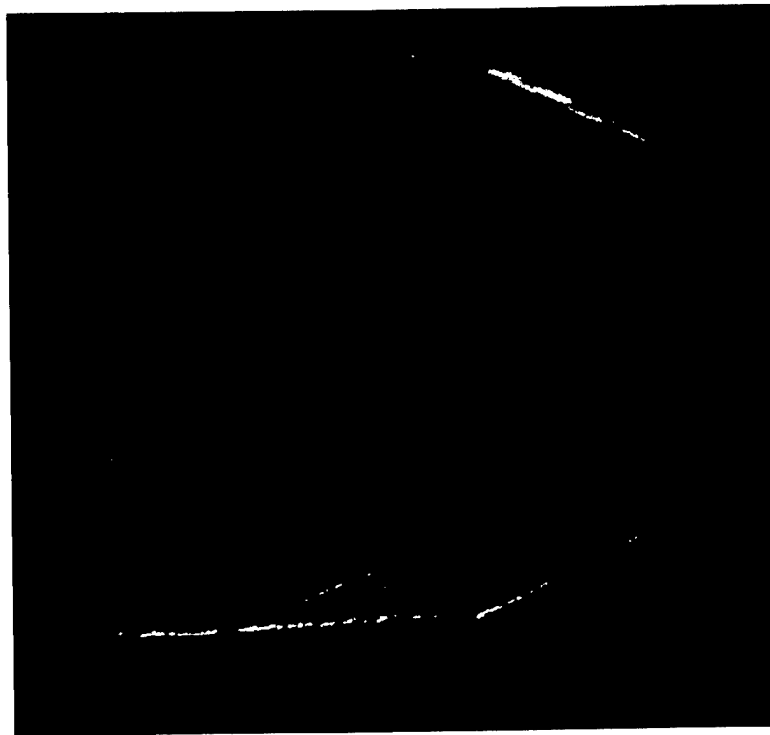


(a) Shadowgraph Photo

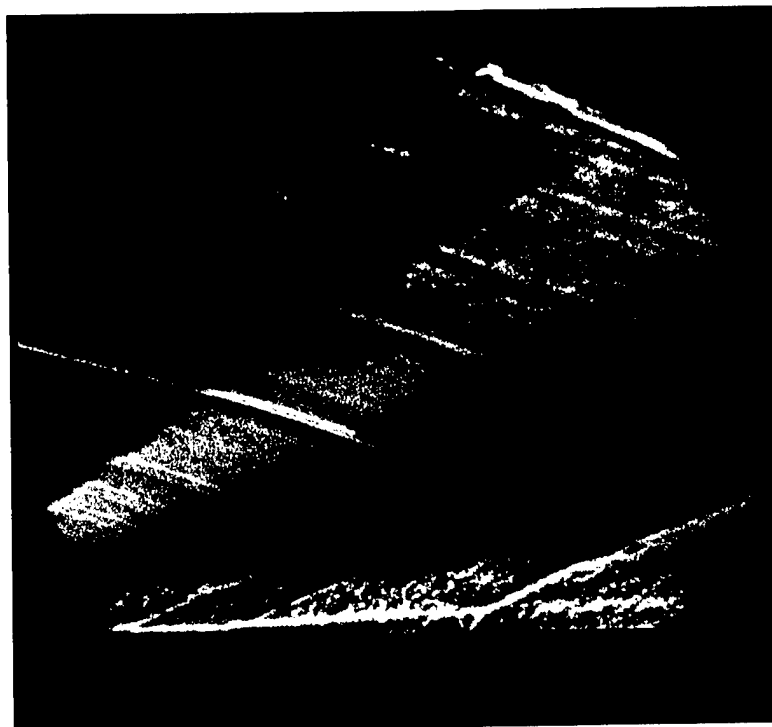


(b) Schlieren Photo

Figure 6.5 Visualizations of LD3-O2-16 (a) Shadowgraph Photo, (b) Schlieren Photo

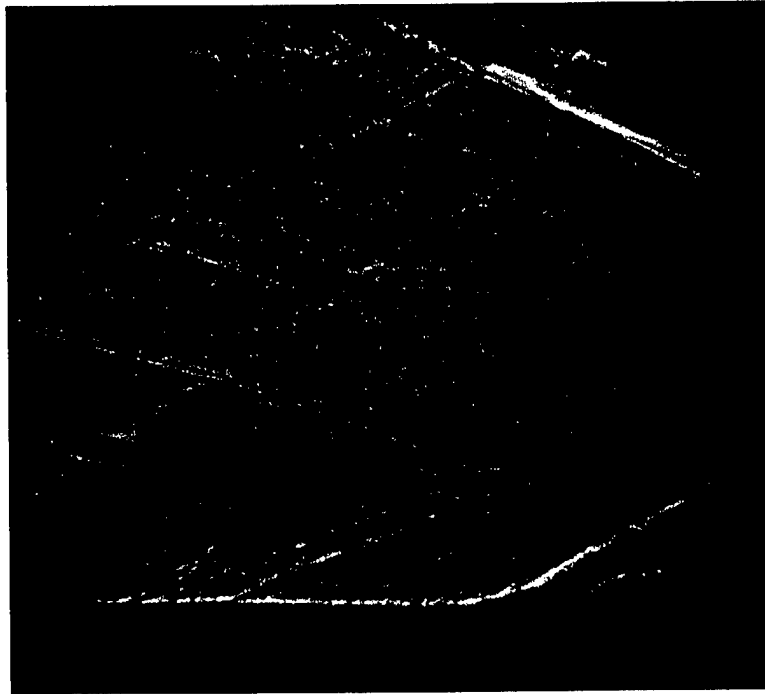


(a) Shadowgraph Photo

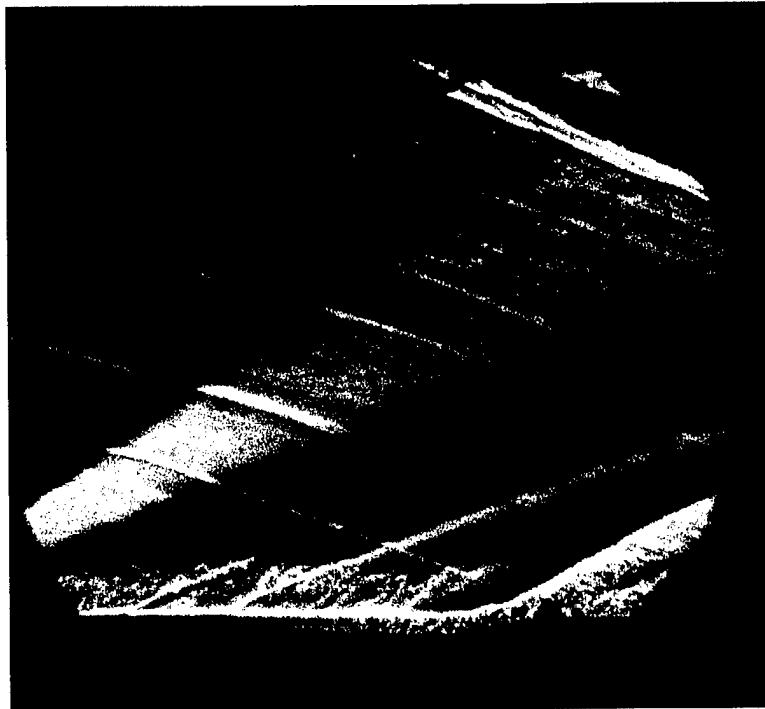


(b) Schlieren Photo

Figure 6.6 Visualizations of LD5-O1 (a) Shadowgraph Photo, (b) Schlieren Photo



(a) Shadowgraph Photo



(b) Schlieren Photo

Figure 6.7 Visualizations of LD5-O1-16 (a) Shadowgraph Photo, (b) Schlieren Photo

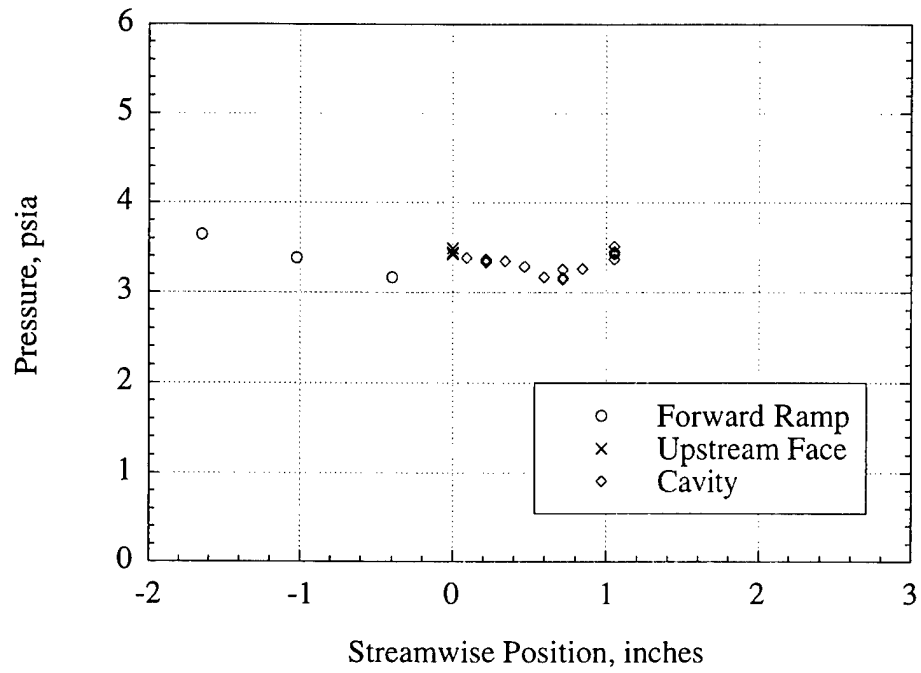


Figure 6.8 Wall Static Pressure Distribution for LD3-O1

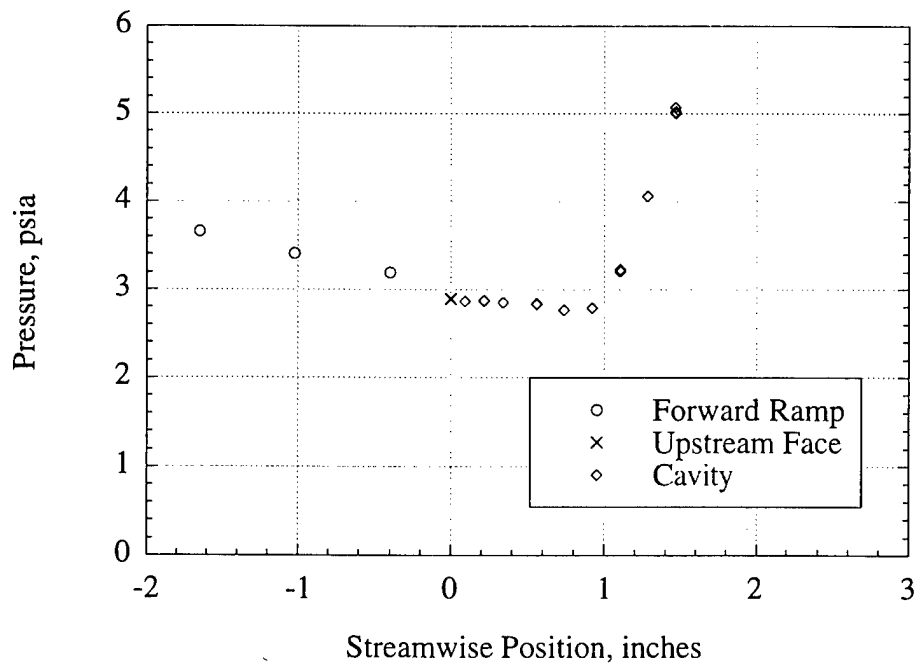


Figure 6.9 Wall Static Pressure Distribution for LD3-O1-16

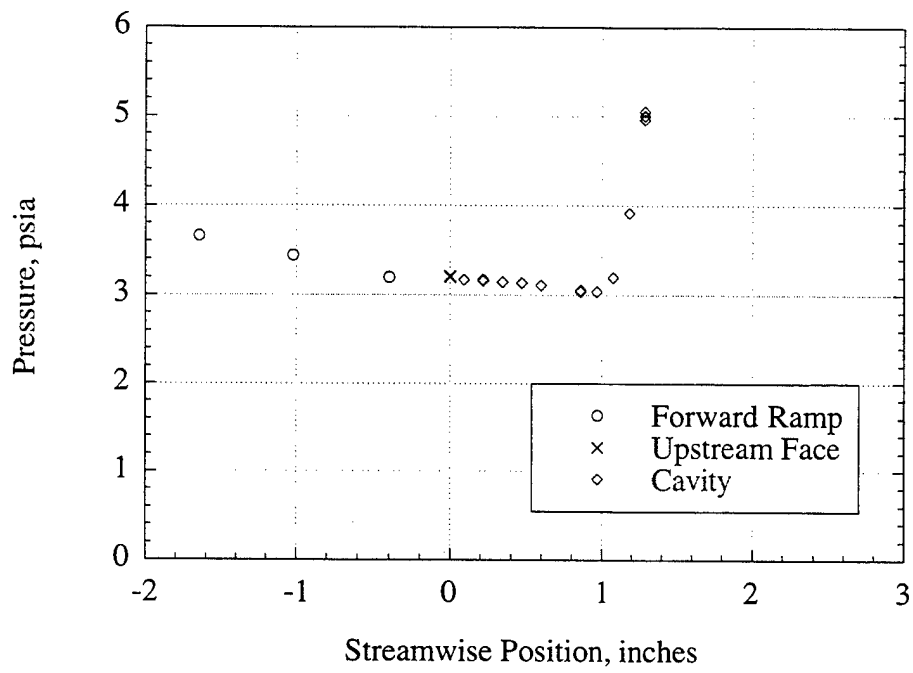


Figure 6.10 Wall Static Pressure Distribution for LD3-O1-30

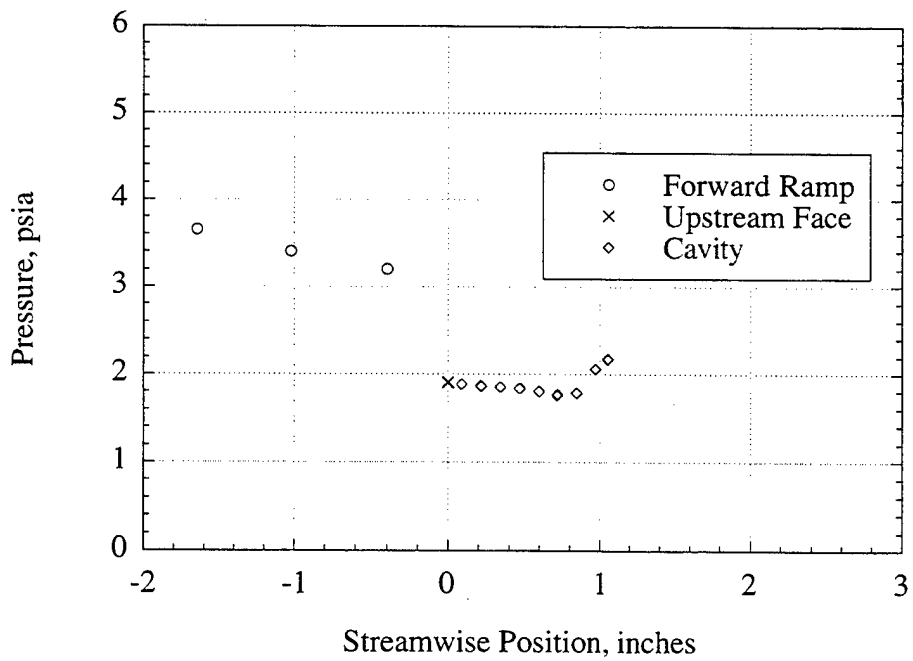


Figure 6.11 Wall Static Pressure Distribution for LD3-O2

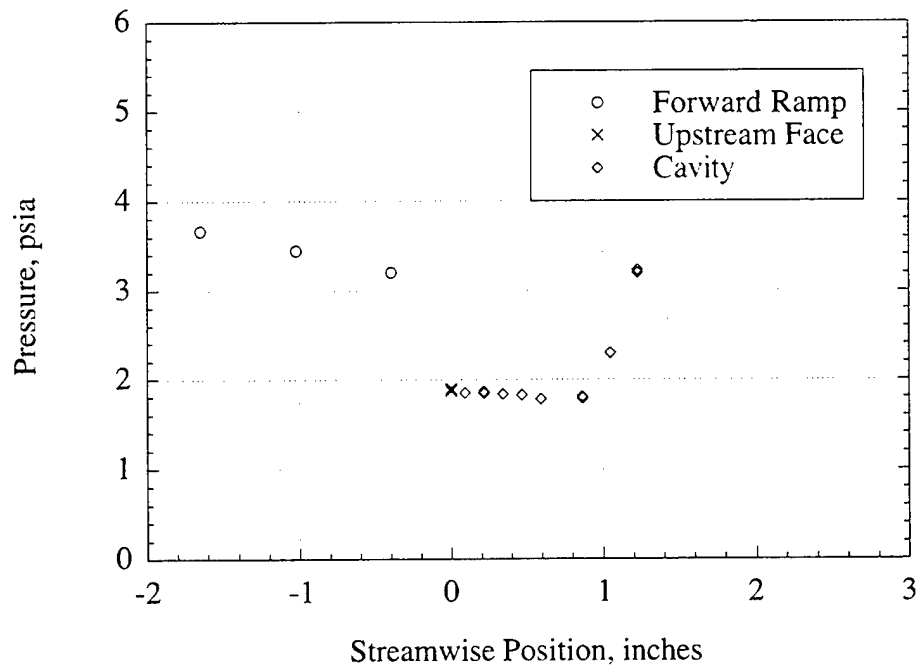


Figure 6.12 Wall Static Pressure Distribution for LD3-O2-16

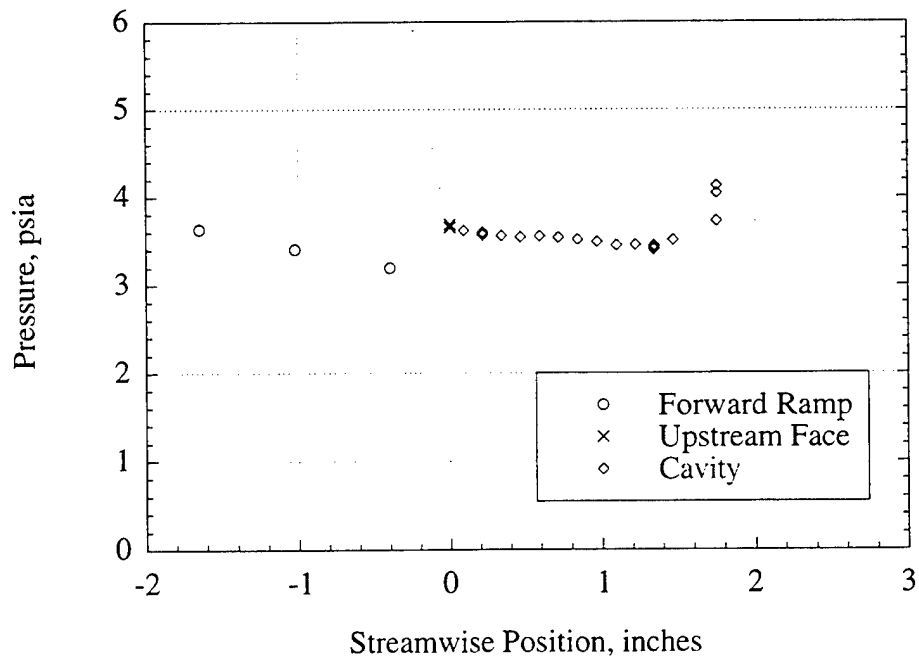


Figure 6.13 Wall Static Pressure Distribution for LD5-O1

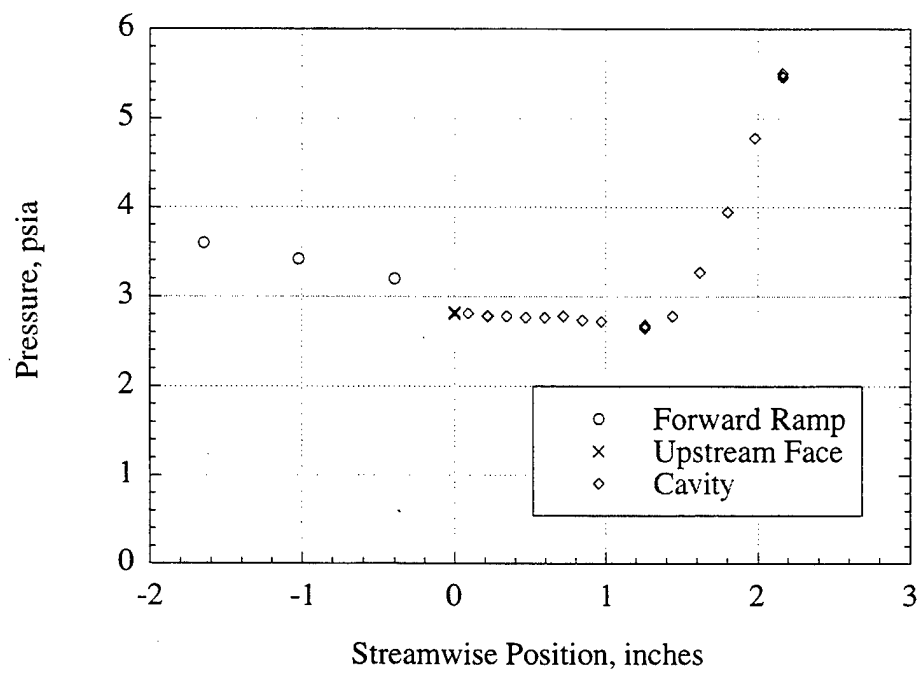


Figure 6.14 Wall Static Pressure Distribution for LD5-O1-16

References

¹Baurle, R. A., and Gruber, M. R., "A Study of Recessed Cavity Flowfields for Supersonic Combustion Applications," AIAA Paper 98-0938, January 1998.

²Ben-Yakar, A., and Hanson, R., "Cavity Flameholders for Ignition and Flame Stabilization in Scramjets: Review and Experimental Study," AIAA Paper 98-3122, July 1998.

³Davis, D. L., "Numerical Analysis of Two and Three Dimensional Recessed Flame Holders for Scramjet Applications," Ph.D. Thesis, Air Force Institute of Technology Air University, WPAFB, OH, 1996.

⁴Baysal, O., and Stallings, R. L., "Computational and Experimental Investigation of Cavity Flowfields," *AIAA Journal*, Vol. 26, No. 1, 1988, pp. 6-7.

⁵Chokani, N., and Kim, I., "Suppression of Pressure Oscillations in an Open Cavity by Passive Pneumatic Control," AIAA Paper 91-1729, June 1991.

⁶Clark, R. L., Kaufmann, L. G., and Maciulaitis, A., "Aeroacoustic Measurements for Mach 0.6 to 3.0 Flows Past Rectangular Cavities," AIAA Paper 80-0036, January 1980.

⁷Edwards, J. A., and Zhang, X., "Some Aspects of Supersonic Flow Over a Cavity," AIAA Paper 86-2025, August 1986.

⁸Franke, M. E., and Carr, D. L., "Effect of Geometry on Open Cavity Flow-Induced Pressure Oscillations," AIAA Paper 75-492, March 1975.

⁹Hankey, W. L., and Shang, J. S., "Analyses of Pressure Oscillations in an Open Cavity," *AIAA Journal*, Vol. 18, No. 8, 1980, pp. 892-898.

¹⁰Jeng, Y. N., and Payne, U. J., "Numerical Study of a Supersonic Open Cavity Flow and Pressure Oscillation Control," *Journal of Aircraft*, Vol. 32, No. 2, 1995, pp. 363-369.

¹¹Kim, I., and Chokani, N., "Navier-Stokes Study of Supersonic Cavity Flowfield with Passive Control," *Journal of Aircraft*, Vol. 29, No. 2, 1992, pp. 217-223.

¹²Komerath, N. M., Ahuja, K. K., and Chambers, F. W., "Prediction and Measurement of Flows Over Cavities--A Survey," AIAA Paper 87-0166, January 1987.

¹³McGregor, O. W., and White, R. A., "Drag of Rectangular Cavities in Supersonic and Transonic Flow Including the Effects of Cavity Resonance," *AIAA Journal*, Vol. 4, No. 11, 1970, pp. 1959-1964.

¹⁴Morgenstern, A., and Chokani, N., "Hypersonic Flow Past Open Cavities," *AIAA Journal*, Vol. 32, No. 12, 1994, pp. 2387-2393.

¹⁵Perng, S. W., and Dolling, D. S., "Passive Control of Pressure Oscillations in Hypersonic Cavity Flow," *AIAA Paper 96-0444*, January 1996.

¹⁶Rizzetta, D. P., "Numerical Simulation of Supersonic Flow Over a Three-Dimensional Cavity," *AIAA Journal*, Vol. 26, No. 7, 1988, pp. 799-807.

¹⁷Rockwell, D., and Naudascher, E., "Review--Self-Sustaining Oscillations of Flow Past Cavities," *Journal of Fluids Engineering*, Vol. 100, No. 6, 1978, pp. 152-165.

¹⁸Sarno, R. L., and Franke, M. E., "Suppression of Flow-Induced Pressure Oscillations in Cavities," *Journal of Aircraft*, Vol. 31, No. 1, 1994, pp. 90-96.

¹⁹Vakili, A. D., Wolfe, R., Nagle, T., and Lambert, E., "Active Control of Cavity Aeroacoustics in High Speed Flows," *AIAA Paper 95-0678*, January 1995.

²⁰Zhang, X., and Edwards, J. A., "Computational Analysis of Unsteady Supersonic Cavity Flows Driven by Thick Shear Layers," *Aeronautical Journal*, Vol. 92, No. 919, 1988, pp. 365-374.

²¹Zhang, X., and Edwards, J. A., "An Investigation of Supersonic Oscillatory Cavity Flows Driven by Thick Shear Layers," *Aeronautical Journal*, Vol. 94, No. 940, 1990, pp. 355-364.

²²Zhang, X., and Edwards, J. A., "Experimental Investigation of Supersonic Flow over Two Cavities in Tandem," *AIAA Journal*, Vol. 30, No. 5, 1992, pp. 1182-1190.

²³Zhang, X., and Edwards, J. A., "A Computational Analysis of Supersonic Jet and Instability Wave Interaction," *AIAA Paper 94-2194*, June 1994.

²⁴Zhang, X., "Compressible Cavity Flow Oscillation due to Shear Layer Instabilities and Pressure Feedback," *AIAA Journal*, Vol. 33, No. 8, 1995, pp. 1404-1411.

²⁵Huellmantel, L. W., Ziemer, R. W., and Cambel, A. B., "Stabilization of Premixed Propane-Air Flames in Recessed Ducts," *ARS Journal*, Vol. No. January, 1957, pp. 31-43.

²⁶Hsu, K. Y., Goss, L. P., Trump, D. D., and Roquemore, W. M., "Performance of a Trapped-Vortex Combustor," AIAA Paper 95-0810, January 1995.

²⁷Katta, V. R., and Roquemore, W. M., "Numerical Studies on Trapped-Vortex Combustor," AIAA Paper 96-2660, July 1996.

²⁸Katta, V. R., and Roquemore, W. M., "Study on Trapped-Vortex Combustor--Effect of Injection on Dynamics of Non-Reacting and Reacting Flows in a Cavity," AIAA Paper 97-3256, July 1997.

²⁹Niioka, T., Terada, K., Kobayashi, H., and Hasegawa, S., "Flame Stabilization Characteristics of Strut Divided into Two Parts in Supersonic Airflow," *Journal of Propulsion and Power*, Vol. 11, No. 1, 1995, pp. 112-116.

³⁰Yu, K., Wilson, K. J., Smith, R. A., and Schadow, K. C., "Experimental Investigation on Dual-Purpose Cavity in Supersonic Reacting Flows," AIAA Paper 98-0723, January 1998.

³¹Vinogradov, V., Grachev, V., Petrov, M., and Sheechman, J., "Experimental Investigation of 2-D Dual Mode Scramjet with Hydrogen Fuel at Mach 4...6," AIAA Paper 90-5269, October 1990.

³²Vinogradov, V., Kobigsky, S., and Petrov, M., "Experimental Investigation of Liquid Carbonhydrogen Fuel Combustion in Channel at Supersonic Velocities," AIAA Paper 92-3426, July 1992.

³³Vinogradov, V. A., Kobigsky, S. A., and Petrov, M. D., "Experimental Investigation of Kerosene Fuel Combustion in Supersonic Flow," *Journal of Propulsion and Power*, Vol. 11, No. 1, 1995, pp. 130-134.

³⁴Romankov, O. N., and Starostin, F. I., "Design and Investigation of the Stand and Flying Scramjet Models Conceptions and Results of Experiments," AIAA Paper 93-2447, June 1993.

³⁵McClinton, C., Roudakov, A., Semenov, V., and Kopehenov, V., "Comparative Flow Path Analysis and Design Assessment of an Axisymmetric Hydrogen Fueled Scramjet Flight Test Engine at a Mach Number of 6.5," AIAA Paper 96-4571, November 1996.

³⁶Nestler, D. E., Saydah, A. R., and Auxer, W. L., "Heat Transfer to Steps and Cavities in Hypersonic Turbulent Flow," AIAA Paper 68-673, June 1968.

³⁷Jackson, K., Gruber, M., Mathur, T., Streby, G., Smith, C., and Billig, F., "Calibration of a Newly Developed Direct-Connect High-Enthalpy Supersonic Combustion Research Facility," AIAA Paper 98-1510, April 1998.

³⁸Gruber, M., Jackson, T., Mathur, T., Jackson, K., and Billig, F., "A Cavity-Based Fuel Injector/Flameholder for Scramjet Applications," Paper Number 2C-07, To Appear at the 1998 Winter JANNAF Meeting 1998.

³⁹Carroll, B. F., Dutton, J. C., and Addy, A. L., "NOZCS2: A Computer Program for the Design of Continuous Slope Supersonic Nozzles," University of Illinois at Urbana-Champaign, UILU ENG 86-4007, 1986.

⁴⁰Burke, A. F., "Turbulent Boundary Layers on Highly Cooled Surfaces at High Mach Numbers," AFASD TR 61-645, 1961.

⁴¹Gruber, M. R., and Nejad, A. S., "Supersonic Combustion Research Laboratory: Volume 1-Design and Fabrication," Wright Laboratory, WL-TR-93-2052, 1993.

⁴²Gruber, M. R., and Nejad, A. S., "New Supersonic Combustion Research Facility," *Journal of Propulsion and Power*, Vol. 11, No. 5, 1995, pp. 1080-1083.

⁴³Little, B. H., and Whipkey, R. R., "Locked Vortex Afterbodies," *Journal of Aircraft*, Vol. 16, No. 5, 1979, pp. 296-302.